Published Online: 5 February, 2019 | Supp Info: http://doi.org/10.1084/jem.20181216
Downloaded from jem.rupress.org on September 16, 2019

JEM Journal of Experimental Medicine

ARTICLE

Type I interferon induces CXCL13 to support ectopic germinal center formation

Alice E. Denton[1], Silvia Innocentin[1], Edward J. Carr[1,2], Barry M. Bradford[3], Fanny Lafouresse[4,5], Neil A. Mabbott[3], Urs Mörbe[6], Burkhard Ludewig[6], Joanna R. Groom[4,5], Kim L. Good-Jacobson[7,8], and Michelle A. Linterman[1]

Ectopic lymphoid structures form in a wide range of inflammatory conditions, including infection, autoimmune disease, and cancer. In the context of infection, this response can be beneficial for the host: influenza A virus infection–induced pulmonary ectopic germinal centers give rise to more broadly cross-reactive antibody responses, thereby generating cross-strain protection. However, despite the ubiquity of ectopic lymphoid structures and their role in both health and disease, little is known about the mechanisms by which inflammation is able to convert a peripheral tissue into one that resembles a secondary lymphoid organ. Here, we show that type I IFN produced after viral infection can induce CXCL13 expression in a phenotypically distinct population of lung fibroblasts, driving CXCR5-dependent recruitment of B cells and initiating ectopic germinal center formation. This identifies type I IFN as a novel inducer of CXCL13, which, in combination with other stimuli, can promote lung remodeling, converting a nonlymphoid tissue into one permissive to functional tertiary lymphoid structure formation.

Introduction

Influenza A virus (IAV) causes respiratory infections that are a significant cause of morbidity and mortality worldwide (Nair et al., 2011; Somes et al., 2018). Current vaccines are an effective prophylactic treatment that limits infection before it takes hold through the induction of strain-specific antibodies. However, what current influenza vaccines lack is the ability to generate antibodies that are cross-protective between IAV strains. It is known that tertiary lymphoid structures (TLSs), which contain germinal centers (GCs), form in the lung after IAV infection, and these pulmonary GCs are an effective way to generate cross-protective humoral immunity (Adachi et al., 2015). Typically, a GC forms in secondary lymphoid organs (SLOs) after infection or immunization. It is a specialized microenvironment that generates long-term immunity through the generation of memory B cells and antibody-secreting plasma cells that are able to provide protection against subsequent infection. A productive GC reaction requires the collaboration of multiple cell types, including B cells, T follicular helper (Tfh) cells, tingible body macrophages, and follicular dendritic cells (FDCs; Vinuesa et al., 2016). Bringing these cells together requires exquisite cellular coordination to ensure that the rare antigen-specific T and B cells are able to interact with each other in the right place and at the right time. The movement of immune cells within the GC is coordinated by mesenchymal stromal cell populations (Denton and Linterman, 2017); GC initiation in SLOs requires fibroblastic reticular cells of the T cell zone (Cremasco et al., 2014; Denton et al., 2014), and its maintenance requires the FDC network within the B cell follicle (Wang et al., 2011). Thus, the interactions between immune cells and stromal cells are central to the formation of the GC and the quality of its output. While vaccines typically induce GCs in SLOs, GCs can also form within nonlymphoid tissues in response to infection and inflammation. In the lung, infection, inhalation of particulate antigens, and pathological inflammation are known to induce lymphocytic aggregates known as inducible bronchus-associated lymphoid tissue (iBALT) that can form in the parenchyma (Moyron-Quiroz et al., 2004; Rangel-Moreno et al., 2006; Foo and Phipps, 2010; Kuroda et al., 2016). These TLSs vary in their cellular composition from loose clusters of T cells to highly organized aggregates that contain GC-like structures (Moyron-Quiroz et al., 2004; Foo and Phipps, 2010; Onodera et al., 2012; Fleige et al., 2014). In the context of IAV infection, lung GCs

[1]Laboratory of Lymphocyte Signalling and Development, Babraham Institute, Cambridge, UK; [2]Department of Medicine, University of Cambridge, Cambridge, UK; [3]The Roslin Institute and the Royal (Dick) School of Veterinary Sciences, University of Edinburgh, Edinburgh, UK; [4]Walter and Eliza Hall Institute of Medical Research, Parkville, Victoria, Australia; [5]Department of Medical Biology, University of Melbourne, Parkville, Victoria, Australia; [6]Institute of Immunobiology, Kantonsspital St. Gallen, St. Gallen, Switzerland; [7]Infection and Immunity Program, Biomedicine Discovery Institute, Monash University, Clayton, Victoria, Australia; [8]Department of Biochemistry and Molecular Biology, Monash University, Clayton, Victoria, Australia.

Correspondence to Michelle A. Linterman: michelle.linterman@babraham.ac.uk; Alice E. Denton: alice.denton@babraham.ac.uk.

© 2019 Denton et al. This article is distributed under the terms of an Attribution–Noncommercial–Share Alike–No Mirror Sites license for the first six months after the publication date (see http://www.rupress.org/terms/). After six months it is available under a Creative Commons License (Attribution–Noncommercial–Share Alike 4.0 International license, as described at https://creativecommons.org/licenses/by-nc-sa/4.0/).

confer protective immunity in the absence of SLO-derived responses (Moyron-Quiroz et al., 2004; Rangel-Moreno et al., 2007) and with reduced immunopathology (Moyron-Quiroz et al., 2004; Foo and Phipps, 2010; Onodera et al., 2012; Fleige et al., 2014). Importantly, the output of lung GCs comprises plasma cells and memory B cells with greater cross-protective potential (Adachi et al., 2015), suggesting that the biology of lung GCs is distinct from that of LN GCs.

Because ectopic GCs can generate these distinct broadly neutralizing protective antibody responses, they represent an interesting area for potential vaccine development. However, despite the near-ubiquitous presence of ectopic GCs in multiple inflammatory states (Pitzalis et al., 2014; Hwang et al., 2016), we know surprisingly little about the mechanisms that drive their formation and/or function, which limits the potential to use this pathway therapeutically. Perhaps the simplest hypothesis is that these ectopic GCs form in a way that is analogous to a nascent LN, via conserved developmental pathways. Here, we show that this is not the case and that a distinct mechanism initiates GCs in the lung after IAV infection. Type I IFN produced in response to infection induces expression of the chemokine C-X-C motif ligand 13 (CXCL13) by lung fibroblasts. This drives C-X-C motif receptor 5 (CXCR5)–dependent recruitment of B cells to the lung to initiate the formation of functional GCs. This study establishes that the early antiviral response initiates a cascade of signaling events that act on local stromal cells to generate an environment permissive to GC formation in the lung.

Results

GC-like structures form in the lung after IAV infection

Following IAV infection, lymphocytic aggregates consisting of T, B, and dendritic cells form in the lung parenchyma (Fleige et al., 2014). To determine whether GC B cells exist in these aggregates, we used *Aidca*$^{cre\text{-}hCD2}$ mice that express human CD2 as a surrogate marker of activation-induced cytidine deaminase (AID), the canonical GC B cell enzyme. We found clusters of hCD2$^+$ B cells in close association with CD3$^+$ T cells (Fig. 1 A). These B cells express both Ki67, a marker of proliferation, and B cell lymphoma 6 (Bcl6), a transcriptional regulator required for GC B cell formation (Vinuesa et al., 2016; Fig. 1 B). The development of pulmonary GC B cells is slightly delayed compared with those in the mediastinal LN (medLN; Fig. 1 C). As the output of the lung GC is not equivalent to that of the medLN (Takahashi et al., 2017), we sought to characterize the lung GC response further. Both lung and medLN GC B cells express GL-7 and CD95 (Fig. S1, A–C), suggesting that lung and LN GC B cells are phenotypically similar. Lung GC B cells were localized in the parenchyma, as they did not bind i.v.-administered anti-CD45 (Anderson et al., 2012; Fig. S1, D and E). To determine whether lung GCs support plasma cell differentiation, we infected *Prdm1*$^{GFP/+}$ mice, in which GFP marks the expression of B lymphocyte–induced maturation protein 1 (Blimp1), a transcription factor involved in terminal differentiation of B cells into plasma cells. After IAV infection, the lungs of these mice contained a population of GFP$^+$ CD138$^+$ plasmablasts (Fig. S1 F), suggesting that plasma cell development accompanies the lung GC response. In SLOs, GC B cells recirculate between the dark zone (DZ), where they proliferate and undergo somatic hypermutation, and the light zone (LZ), where they receive survival and selection signals from FDCs and Tfh cells (Denton and Linterman, 2017). The proportion of LZ CXCR4^{low}CD86^{hi} B cells is increased in the lung relative to the medLN (Fig. 1, D–F). Confocal microscopy analysis revealed distinguishable LZ and DZ areas in lung GCs, alongside rare CD35$^+$ FDCs (Fig. 1 G). Taken together, these data suggest that while lung GC B cells are phenotypically similar to LN GC, differences in LZ/DZ partitioning are evident at these two sites, perhaps due to altered selection efficiency. This prompts the hypothesis that there may be differences in the provision of T cell help in lung GCs. However, which T cells provide help in IAV-induced lung GCs is not known. We identified a population of CXCR5^{high}PD-1^{high}Bcl6$^+$CD4$^+$Foxp3$^-$ cells in the IAV-infected lung that phenotypically resemble Tfh cells (Fig. 1 H), suggesting that these cells may be the source of T cell help for GC B cells in the lung.

Tfh cells are required for lung GC formation

To determine if the presence of Tfh-like cells in the lung after IAV infection is functionally relevant, we tested whether lung GCs need T cell help to form. Lung GCs were absent in mice that lack αβ T cells (*Tcra*$^{-/-}$ mice; Fig. 2 A). The number of Tfh cells correlates positively with the number of GC B cells in the medLN (Fig. 2 B) and lung (Fig. 2 C), consistent with interdependence of these two cell types. To formally test the requirement for Tfh-like cells, we infected Tfh cell–deficient (*Bcl6*$^{fl/fl}$ *Cd4*$^{cre/+}$) animals with IAV and found a complete lack of GC B cells in the lung (Fig. 2, D–F). In *Sh2d1a*$^{-/-}$ mice, which have defective Tfh cell development (Qi et al., 2008), lung GC formation was also impaired (Fig. 2 G). By contrast, *Tbx21*$^{fl/fl}$ *Cd4*$^{cre/+}$ mice, which lack Th1 cells (Fig. 2, H and I), have intact lung Tfh cell and GC B cell responses (Fig. 2, J and K), suggesting that the provision of help to lung GC B cells comes specifically from lung Tfh cells.

GC B cells compete with each other for access to T cell–derived help in the form of receptor-mediated costimulation and cytokines, such as CD40L and IL-21. B cells that bind antigen and receive help from Tfh cells acquire expression of c-Myc, promoting their survival and proliferation (Calado et al., 2012; Dominguez-Sola et al., 2012; Luo et al., 2018). Gain of c-Myc expression by GC B cells is therefore a functional readout of competent T cell help. To determine if lung Tfh cells are able to provide help to lung GC B cells, we infected *Cmyc*^{GFP} mice (Huang et al., 2008) with IAV. We found that the frequency of c-Myc–expressing GC B cells is lower in the lung than in the medLN (Fig. 2, L and M), indicating that while positive selection of GC B cells occurs in the lung, the process is less efficient than in the draining medLN. We also investigated whether the Tfh-like T cells in the lung were bona fide Tfh or Tfh precursors by IL-7Rα staining (Lim and Kim, 2007) and found that the proportion of IL-7Rα$^+$ cells among the CXCR5$^+$PD-1$^+$ Tfh cells was not different between the medLN and lung (Fig. 2 N). Despite the subtle differences in T cell–mediated selection and DZ/LZ phenotype in lung GC B cells compared with LN GC B cells, the data obtained thus far indicate that the pulmonary GCs induced by

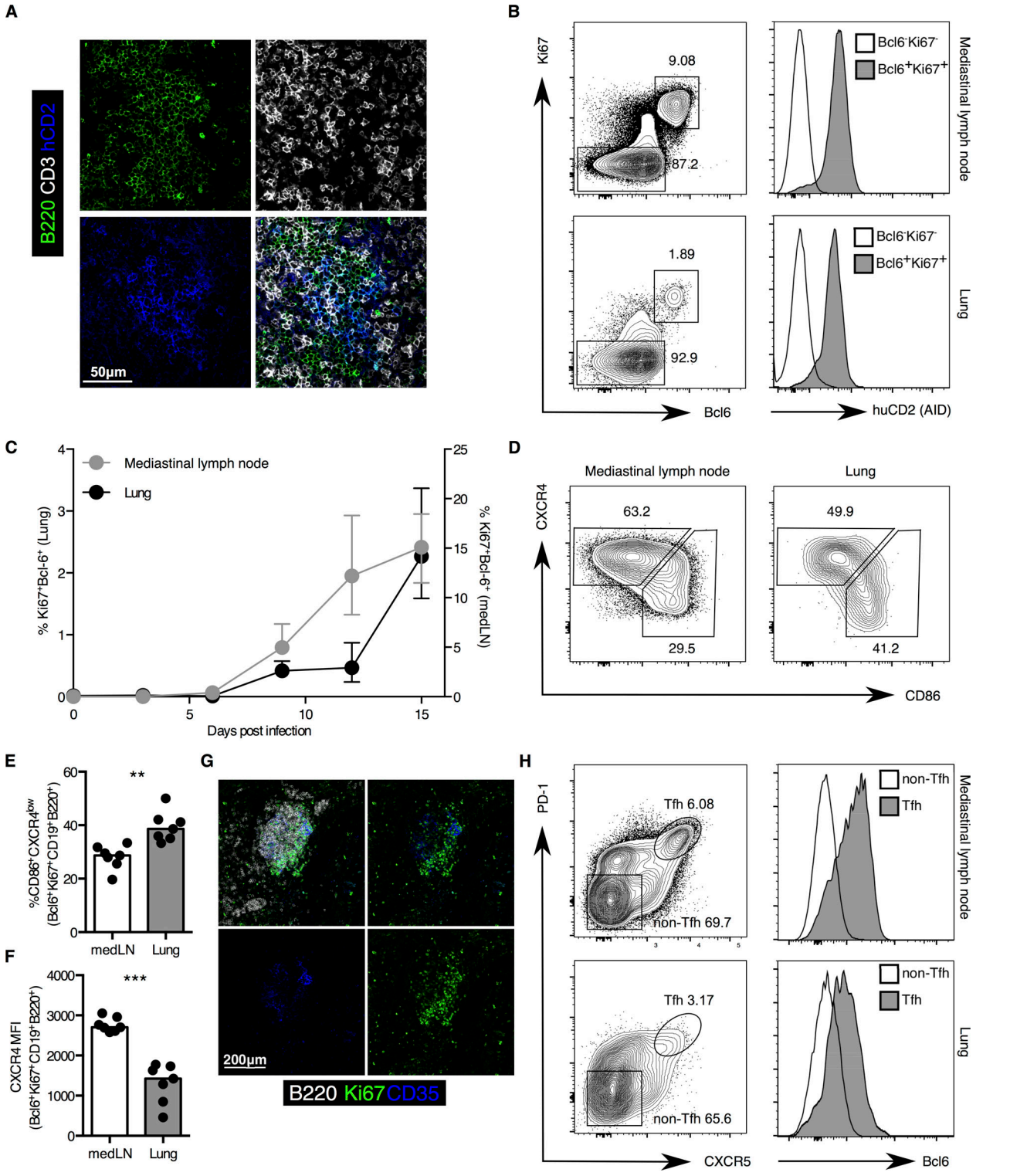

Figure 1. **GCs are induced in the lung after IAV infection. (A)** Confocal image of B220 (green), CD3 (white), and AID (huCD2, blue) staining in lung tissue 14 d after IAV infection. Scale bar, 50 µm. **(B)** Flow cytometric plots identifying Bcl6⁺Ki67⁺AID⁺ GC B cells in the draining medLN and lung 14 d after IAV infection. **(C)** Quantification of Bcl6⁺Ki67⁺AID⁺ GC B cells (expressed as a percentage of B cells) at indicated time points after IAV infection; symbols show the median, and error bars show the interquartile range. **(A–C)** Representative of two independent experiments with four to six mice per group. **(D–F)** Flow cytometric plots and quantification of LZ and DZ phenotype Bcl6⁺Ki67⁺B220⁺CD19⁺ GC B cells in the medLN and lung 14 d after IAV infection. Numbers in D indicate the proportion of LZ (CXCR4⁺CD86⁻) and DZ (CXCR4⁻CD86⁺) cells among GC B cells. Representative of two independent experiments with six or seven mice per group. **(G)** Confocal image of B220 (white), CD35 (blue), and Ki67 (green) staining in lung tissue 14 d after IAV infection. Scale bar, 200 µm. Representative of two independent experiments with four mice per group. **(H)** Flow cytometric plots identifying Bcl6⁺CXCR5⁺PD-1⁺CD4⁺Foxp3⁻ Tfh cells in the draining medLN and lung 14 d after IAV infection. Numbers indicate the proportion of Tfh (CXCR5⁺PD-1⁺) or non-Tfh (CXCR5⁻PD-1⁻) cells among T cells. In bar plots, the height of the bar is the median, and each symbol represents one biological replicate. Representative of four independent experiments with four to eight mice per group. Statistical significance was determined with a two-sided Mann–Whitney *U* test (**, P < 0.01; ***, P < 0.001).

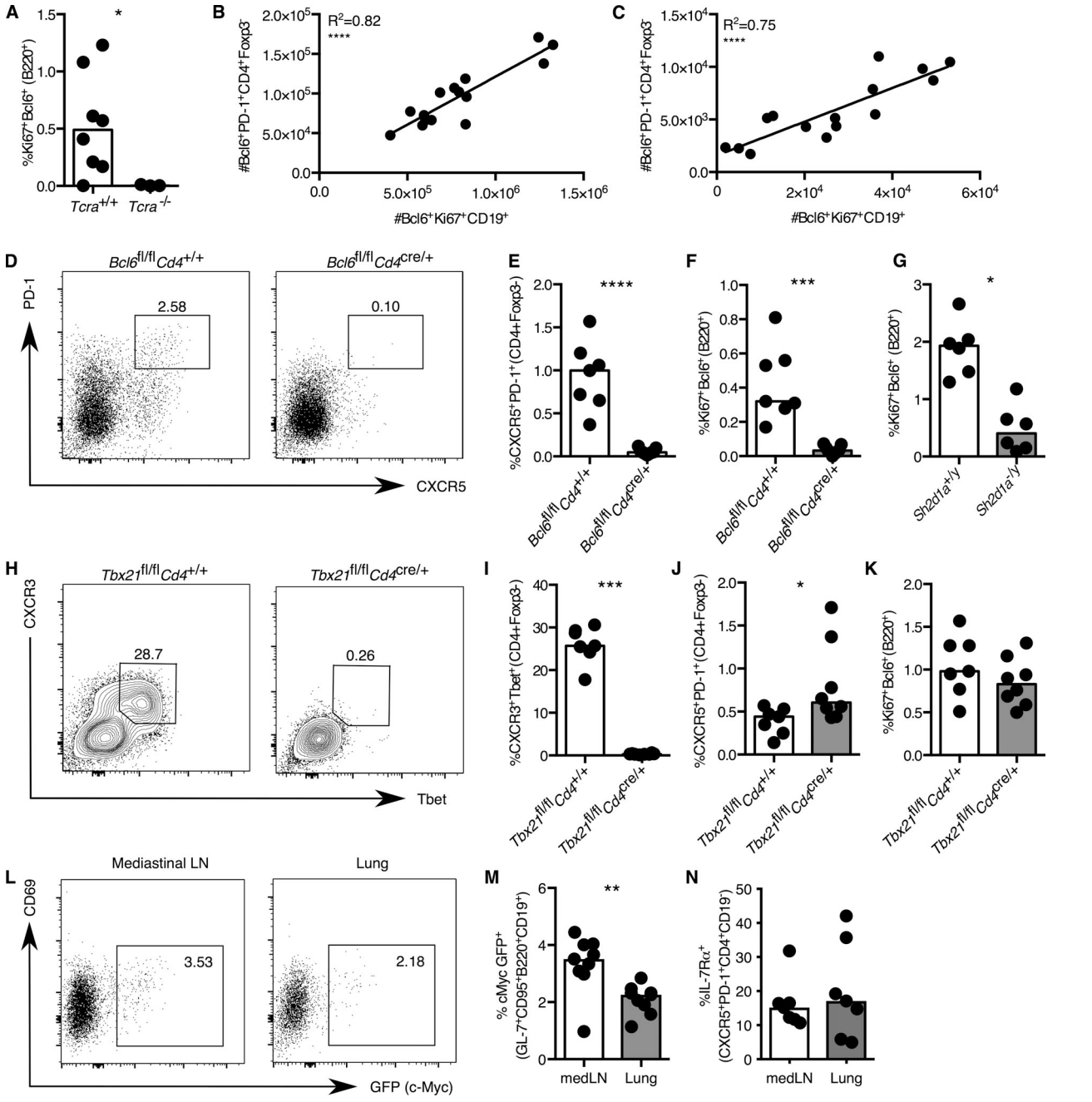

Figure 2. **Tfh cells are required for lung GC formation. (A)** Quantification by flow cytometry of lung Bcl6$^+$Ki67$^+$CD19$^+$ GC B cells (expressed as a percentage of B cells) in *Tcra*$^{-/-}$ and control C57BL/6 mice 14 d after IAV infection. Representative of two independent experiments with three to eight mice per group. **(B and C)** Correlation of Bcl6$^+$Ki67$^+$CD19$^+$ GC B cells and Bcl6$^+$PD-1$^+$CD4$^+$Foxp3$^-$ Tfh cells in the medLN (B; R^2 = 0.82, P < 0.0001) and lung (C; R^2 = 0.75, P < 0.0001) 14 d after IAV infection. R^2 and P values were calculated using Pearson correlation coefficient. Data are representative of three independent experiments with 15–16 mice per group. **(D–F)** Flow cytometric dot plots (D) and quantification of CXCR5$^+$PD-1$^+$CD4$^+$Foxp3$^-$ Tfh cells (E) and Bcl6$^+$Ki67$^+$CD19$^+$ GC B cells (F) in the lung 14 d after IAV infection of *Bcl6*$^{fl/fl}$*Cd4*$^{cre/+}$ mice and *Bcl6*$^{fl/fl}$*Cd4*$^{+/+}$ littermate controls. Numbers in D indicate the proportion of CXCR5$^+$PD-1$^+$ Tfh cells among T cells. Data are representative of three independent experiments with six to eight mice per group. **(G)** Quantification of Bcl6$^+$Ki67$^+$CD19$^+$ GC B cells in the lung 14 d after IAV infection of *Sh2d1a*$^{-/y}$ mice and *Sh2d1a*$^{+/y}$ littermate controls. Data are representative of two independent experiments with six mice per group. **(H–J)** Flow cytometric contour plots (H) and quantification of CXCR3$^+$Tbet$^+$CD4$^+$Foxp3$^-$ Th1 cells (I), CXCR5$^+$PD-1$^+$CD4$^+$Foxp3$^-$ Tfh cells (J), and Bcl6$^+$Ki67$^+$CD19$^+$ GC B cells (K) in the lung 14 d after IAV infection of *Tbx21*$^{fl/fl}$ *Cd4*$^{cre/+}$ mice and *Tbx21*$^{fl/fl}$ *Cd4*$^{+/+}$ littermate controls. Numbers in H indicate the proportion of CXCR3$^+$T-bet$^+$ cells among T cells. Data are representative of three independent experiments with six to eight mice per group. **(L and M)** Flow cytometric dot plots (L) and quantification of the proportion of GL-7$^+$CD38$^-$B220$^+$CD19$^+$ GC B cells (M) expressing c-Myc (GFP) in the medLN and lung 14 d after IAV infection. Numbers in L indicate the proportion of GFP$^+$ (c-Myc$^+$) cells among GC B cells. Data are representative of three independent experiments with four to eight mice per group. **(N)** Proportion of IL-7Rα$^+$ cells among CXCR5$^+$PD-1$^+$CD4$^+$ Tfh cells in the medLN and lung 14 d after IAV infection. Data are representative of two independent experiments with six or seven mice per group. In bar plots, the height of the bar is the median, and each symbol represents one biological replicate. Statistical significance was determined with a two-sided Mann–Whitney *U* test (*, P < 0.05; **, P < 0.01; ***, P < 0.001; ****, P < 0.0001).

viral infection are largely similar to those observed in the LN, albeit with a distinct antibody output (Adachi et al., 2015).

Within SLOs, GC structure is largely driven by oxysterol and chemokine-derived signals that coordinate B and T cell localization and movement, and these ligands are produced by specialized mesenchymal stromal cell types within the SLO, such as FDCs (Wang et al., 2011; Denton et al., 2014; Denton and Linterman, 2017). Because the lungs do not have this specialized stromal cell network, IAV infection must induce remodeling of lung tissue first to recruit, and then to organize, lymphocytes into functional GC-like structures.

CXCR5–CXCL13 signaling drives B cell recruitment to the lung after infection

The first step required for the initiation of a GC is the recruitment of antigen-specific T and B cells. To understand how this is controlled in the lung after IAV infection, we monitored recruitment of $CD4^+$ T cells and B cells to the lung parenchyma by labeling vascular hematopoietic cells with i.v.-injected anti-CD45 (Fig. S1, D and E). In the absence of infection, the majority of T and B cells in the lung are in the blood vessels; after infection, cells are recruited into the parenchyma with infiltration, peaking 6 d after infection for B cells and 9 d after infection for $CD4^+$ T cells (Fig. 3, A and B). To determine what signals control B cell recruitment to the lung, we first considered the role of CXCR3, which is expressed by some B cell subsets after activation (www.immgen.org) and by iBALT B cells in chronic obstructive pulmonary disease (COPD) patients (Kelsen et al., 2009). Furthermore, the CXCR3 ligands CXCL9 (MIG), CXCL10 (IP-10), and CXCL11 (I-TAC) are induced by IAV infection (Groom and Luster, 2011). However, $Cxcr3^{fl/fl}$ $Tg(Fcer2a^{cre})$ animals that lack CXCR3 specifically on mature B cells (Fig. S2 A) do not have impaired B cell migration to the lung following IAV infection (Fig. 3 C). This led us to speculate that naive B cells may be directly recruited to the lung and activated locally. To test this hypothesis, we assessed whether B cells specific for an antigen irrelevant to IAV, hen egg lysozyme (HEL), can be recruited to the lung after IAV infection. We infected SW_{HEL} mice (Phan et al., 2003), in which 10–30% of B cells have a B cell receptor specific for HEL, with IAV and found that HEL-binding B cells entered the lung parenchyma at the same frequency as polyclonal B cells (Fig. 3 D). This demonstrates that B cells do not require antigen-mediated activation before entry into the lung, suggesting that recruitment to the lung may be independent of activation in the LN. To determine whether B cells are activated in the LN before entry to the lung, we lethally irradiated $Rag2^{-/-}Il2rg^{-/-}$ mice and reconstituted them with WT bone marrow (BM) to generate mice with a full complement of immune cells but lacking LNs. In these mice, B cells are not compromised in their ability to enter the lung parenchyma 5 d after IAV infection. Rather, an increased proportion of B cells could enter the lung in the absence of LNs (Fig. 3 E). In support of this notion, prevention of lymphocyte egress from SLOs by treatment with the S1P receptor agonist FTY720 reduces the number of B cells in the lung vasculature, but not in the lung parenchyma (Fig. 3, F and G). Taken together, these data demonstrate that B cell recruitment to the lung following IAV infection is independent of LN trafficking and B cell receptor signaling.

The entry of naive B cells into SLOs is antigen independent and driven by the chemokines C-C motif ligand 19 (CCL19), CCL21, CXCL12, and CXCL13, which are produced by the stromal cell network within the lymphoid tissues (Förster et al., 1999; Okada et al., 2002; Denton and Linterman, 2017). While these chemokines are constitutively expressed in SLOs, they are not abundantly expressed in the naive lung. Rather, chemokines such as CXCL13 and CCL21 are induced in the lung after IAV infection (Moyron-Quiroz et al., 2004). We hypothesized that, in order to recruit naive B cells to initiate a GC in the lung, IAV infection induces expression of these chemokines in local mesenchymal cells. We confirmed that *Cxcl13* and *Ccl19* are induced in the lung following IAV infection, with expression of mRNA peaking 5–6 d after infection (Fig. 3 H), before formation of GC-like iBALT structures. To determine if B cell entry in the lung is driven by responsiveness to C-C motif receptor 7 (CCR7) ligands (CCL19 and CCL21), we generated BM chimeras in which all B cells lacked CCR7 expression (B:$Ccr7^{-/-}$). Following IAV infection, B cell trafficking into the lung parenchyma (CD45i.v.-negative B cells) was equivalent between control chimeras and those in which B cells lack CCR7 expression (Fig. 3 I), demonstrating that CCR7 is not necessary for B cell trafficking to the lung. Finally, we excluded a role for Tfh cells in directing B cell trafficking into the lung following IAV infection, as $Cd4^{cre/+}Bcl6^{fl/fl}$ animals, which lack Tfh cells, showed no change in the proportion of B cells that had entered the lung parenchyma or the induction of *Cxcl13* mRNA 6 d after IAV infection (Fig. S2, B and C).

To determine whether B cell entry to the lung requires CXCR5-dependent migration toward infection-induced CXCL13, we generated mice in which mature B cells specifically lack CXCR5, namely $Cxcr5^{fl/fl}$ $Tg(Fcer2a^{cre})$ mice. 6 d after IAV infection, B cell recruitment into the lung is impaired in these mice (Fig. 3 J). Because the frequency of B cells in the lung parenchyma of uninfected $Cxcr5^{fl/fl}$ $Tg(Fcer2a^{cre})$ mice is similar to that of control animals (Fig. 3 K), these data demonstrate that during infection with IAV, CXCR5 is required by B cells for their migration into the lung.

To determine the impact of impaired B cell recruitment on the formation of lung GCs, we assessed B cell responses in $Cxcr5^{fl/fl}$ $Tg(Fcer2a^{cre})$ mice 14 d after IAV infection. Consistent with the day 6 data (Fig. 3 I), the frequency of B cells in the lung parenchyma was reduced in $Cxcr5^{fl/fl}$ $Tg(Fcer2a^{cre})$ mice compared with controls (Fig. 4, A and B), as was the proportion of GC B cells (Fig. 4 C), demonstrating that CXCR5 is important for the GC B cell response in the lung. Because CXCR5 contributes to B cell migration in SLOs (Förster et al., 1996), we also inhibited CXCL13 in WT mice to exclude any potential artifacts due to altered development and/or homeostasis of CXCR5-deficient B cells. We administered a CXCL13 blocking antibody (Klimatcheva et al., 2015) on days 0, 3, 7, and 10 after IAV infection (Fig. 4 D). This treatment left GC responses intact in the draining medLN 14 d after IAV infection (Fig. 4 E), but both B cell recruitment to and GC formation within the lung were reduced in anti-CXCL13–treated mice (Fig. 4, F and G). While

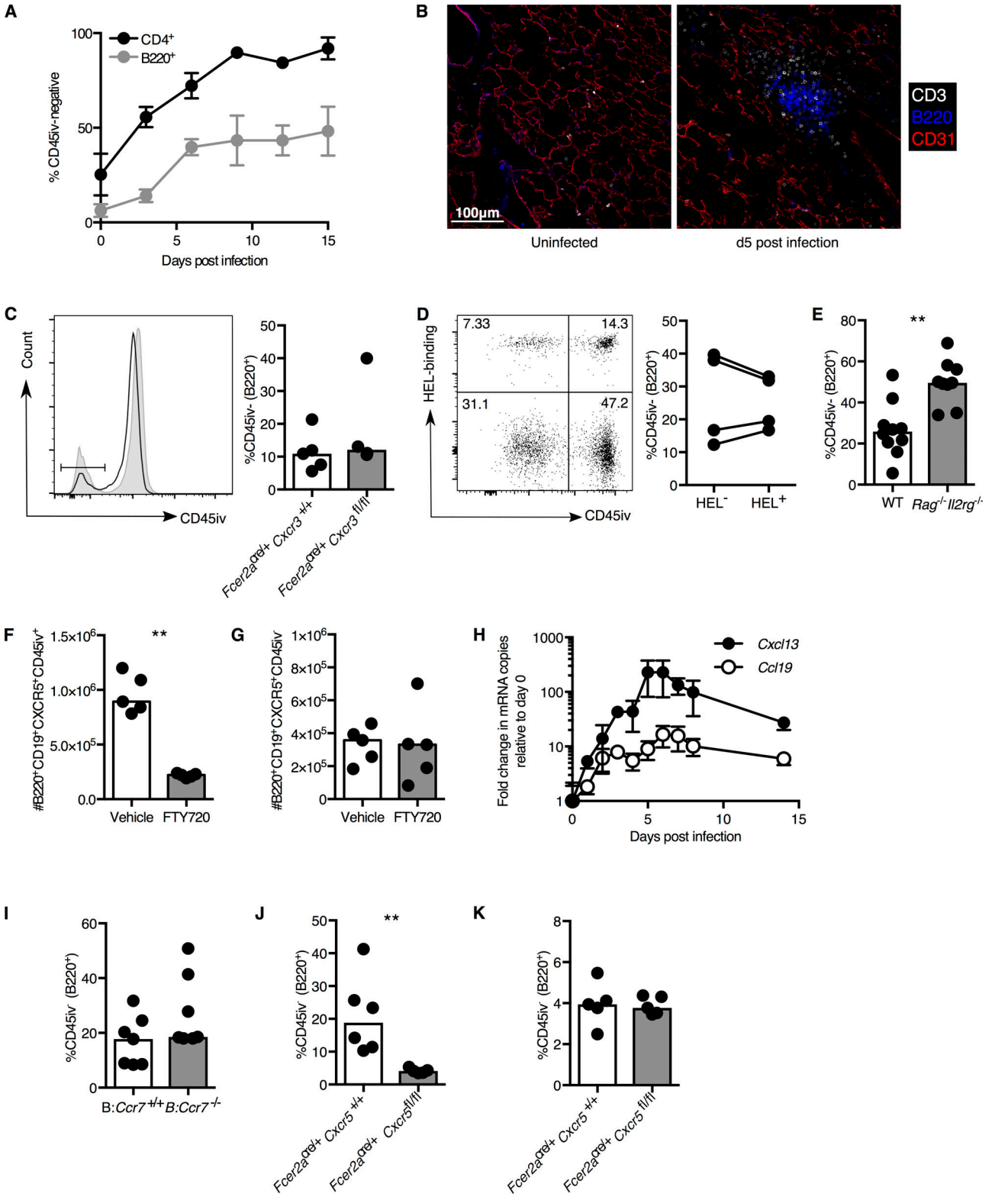

Figure 3. **De novo induction of *Cxcl13* recruits B cells into the lung after IAV infection. (A)** Proportion of CD4+ T cells and B220+ B cells in the lung parenchyma at the indicated days after IAV infection. Parenchymal lymphocytes are defined as those that do not bind anti-CD45 administered i.v. 3 min before euthanasia. **(B)** Confocal images of CD31+ blood vessels (red), CD3+ T cells (white), and B220+ B cells (blue) at indicated days after IAV infection. Scale bar, 100 µm. **(A and B)** Data are representative of two independent experiments with five mice per group. **(C)** Flow cytometric histogram and quantification of CD45i.v.−B220+CD19+ B cells in the lung 6 d after IAV infection of *Cxcr3*$^{fl/fl}$ *Tg(Fcer2a*^{cre}*)* mice and *Cxcr3*$^{+/+}$ *Tg(Fcer2a*^{cre}*)* control mice. Data are representative of two independent experiments with four or five mice per group. **(D)** Representative flow cytometric dot plot, and proportions of polyclonal or HEL-binding B220+CD19+ B cells that are CD45i.v.− in the lung 6 d after IAV infection of SW_{HEL} mice. Numbers indicate the proportion of cells within each quadrant among

B220$^+$CD19$^+$ B cells. Data are representative of two independent experiments with four mice per group. **(E)** Proportion of parenchymal B cells, as determined by lack of CD45i.v. labeling, in either WT or *Rag2*$^{-/-}$*Il2rg*$^{-/-}$ mice that have been irradiated and reconstituted with WT BM 8 wk before infection. Data are representative of two independent experiments with 8–10 mice per group. **(F and G)** Number of B cells in the blood (F; CD45i.v.$^+$B220$^+$CD19$^+$CXCR5$^+$) or the lung parenchyma (G; CD45i.v.$^-$B220$^+$CD19$^+$CXCR5$^+$) 6 d after IAV infection, where FTY720 was administered on days 3 and 5 after IAV infection. Data are representative of two independent experiments with five mice per group. **(H)** Quantitative RT-PCR detection of *Cxcl13* and *Ccl19* transcripts in whole-lung mRNA at the indicated days after IAV infection. Data are representative of two independent experiments with three mice per group. **(I)** Quantification of CD45i.v.$^-$B220$^+$CD19$^+$ B cells in the lung parenchyma 6 d after IAV infection of B:*Ccr7*$^{-/-}$ chimeras and control B:*Ccr7*$^{+/+}$ chimeras. Data are representative of two independent experiments with six to eight mice per group. **(J)** Quantification of CD45i.v.$^-$B220$^+$CD19$^+$ B cells in the lung parenchyma 6 d after IAV infection of *Cxcr5*$^{fl/fl}$ *Tg(Fcer2a*^{cre}*)* mice and *Cxcr5*$^{+/+}$ *Tg(Fcer2a*^{cre}*)* control mice. Data are representative of five independent experiments with four to seven mice per group. **(K)** Quantification of CD45i.v.$^-$B220$^+$CD19$^+$ B cells in the lung parenchyma in uninfected *Cxcr5*$^{fl/fl}$ *Tg(Fcer2a*^{cre}*)* mice and *Cxcr5*$^{+/+}$ *Tg(Fcer2a*^{cre}*)* control mice. Data are representative of two independent experiments with five mice per group. In A and H, each symbol represents the median; the error bars show standard deviation. In bar plots, the height of the bar is the median, and each symbol represents one biological replicate. In C and E–K, statistical significance was determined with a two-sided Mann-Whitney *U* test. In D, the P value was calculated using a paired *t* test and is representative of two independent experiments. **, P < 0.01.

the total GC B cell frequency was not altered in the medLN following anti-CXCL13 treatment (Fig. 4 E), the medLN GC structure exhibited subtle changes (Fig. 4 H). The GC was slightly larger in area (Fig. 4 I), in most part due to expansion of the DZ (Fig. 4 J) in anti-CXCL13–treated mice. Thus, B cell trafficking to the lung and subsequent GC formation at this site occur independently of GC responses in the draining LN but require CXCR5–CXCL13 signaling.

These results also raise the question of whether CXCR5 is required solely for B cell migration to the lung or whether CXCR5–CXCL13 signaling has a direct role in GC organization within the lung. To test whether CXCL13 is required for lung GC maintenance, we administered a CXCL13-blocking antibody on days 14 and 17 relative to IAV infection (Fig. 4 K). 20 d after infection, B cell recruitment to the lung is unaffected (Fig. 4 L), as is the frequency of lung GC B cells (Fig. 4 M). Consistent with this observation, GC B cell frequency in the lung of *Cxcr5*$^{fl/fl}$ *Tg(Fcer2a*^{cre}*)* mice is equivalent to controls when assessed as a proportion of those B cells that have entered the lung parenchyma (Fig. 4 N). Taken together, these data demonstrate that CXCL13 promotes the recruitment of B cells to the lung but is dispensable for lung GC maintenance once B cells have entered the lung parenchyma.

IAV infection induces CXCL13 expression in pulmonary fibroblasts

To understand how CXCL13 is induced in the lung after IAV infection, we sought to identify the pulmonary cell type in which it is expressed. 5 d after infection, *Cxcl13* mRNA is increased in lung platelet-derived growth factor receptor α (PDGFRα)$^+$ fibroblasts, but not hematopoietic cells, epithelial cells, or endothelial cells, relative to uninfected controls (Fig. 5 A; the gating strategy is shown in Fig. S3). We also observed that B cell clusters were typically localized around CXCL13-expressing stromal cells in IAV-infected Tg(*Cxcl13*$^{cre\text{-}dTomato}$) mice (Onder et al., 2017; Fig. 5 B). Flow cytometry analysis confirmed that the CXCL13-expressing cells are PDGRFα$^+$ fibroblasts that also express podoplanin (gp38), a signature molecule of immunomodulatory fibroblasts within SLOs (Acton et al., 2014; Fig. 5, C and D).

To determine whether CXCL13-expressing pulmonary fibroblasts were phenotypically distinct from those not expressing CXCL13, we characterized the expression of six common stromal cell markers (gp38, PDGFRα, CD21/35, MHC II, Sca1, and CD44) on CD45$^-$CD31$^-$PDGFRα$^+$CXCL13$^+$ and CD45$^-$CD31$^-$PDGFRα$^+$CXCL13$^-$ cells isolated from lungs of mice infected with IAV 5 or 14 d earlier. CD21/35 is the canonical marker for LN FDCs; Sca1 and CD44 can be used to define mesenchymal stem/stromal cells, although their exact functions are yet to be determined. While the expression of PDGFRα was not different between the two populations, pulmonary CXCL13$^+$ fibroblasts expressed slightly but significantly higher levels of gp38 and Sca1 relative to CXCL13$^-$ fibroblasts both 5 and 14 d after IAV infection (Fig. 5 E). Strikingly, 99% of CXCL13$^+$ fibroblasts did not express the FDC marker CD21/35, indicating that they are not FDC-like (Fig. 5 F), even though CD35$^+$ FDC-like cells can be found in IAV-induced pulmonary GCs (Fig. 1 H). CXCL13$^+$ fibroblasts also had lower levels of MHC II and greater levels of CD44 relative to CXCL13$^-$ fibroblasts both 5 and 14 d after IAV infection (Fig. 5 F). Taken together, these data demonstrate that pulmonary CXCL13$^+$ fibroblasts are not FDC-like and are phenotypically distinct from total lung fibroblasts.

Since CXCL13-expressing fibroblasts are barely detectable in uninfected mice, CXCL13 expression must be induced de novo in the lung after IAV infection. Induction of *Cxcl13* mRNA is independent of T, B, or innate lymphoid cells, as *Rag2*$^{-/-}$*Il2rg*$^{-/-}$ and control mice have similar expression of *Cxcl13* mRNA following IAV infection (Fig. 6 A), suggesting an early inflammatory mediator may be involved. To implicate a soluble mediator in *Cxcl13* induction, we next assessed the expression kinetics of cytokine mRNAs that are induced after IAV infection in a whole-lung transcriptome dataset where samples had been assessed over a time course of infection (Oslund and Baumgarth, 2011; Pommerenke et al., 2012). The induction of mRNAs encoding IL-6 and IFNβ preceded *Cxcl13* expression (Fig. 6 B), while genes encoding IL-1β, type III IFNs, granulocyte colony-stimulating factor, TNF, and IFNγ were all induced early after IAV infection, albeit with a similar expression pattern to *Cxcl13* (Fig. 6 B). This expression pattern indicated that these cytokines may be causal in inducing *Cxcl13* in lung fibroblasts after IAV infection. In vitro, IFNα and IFNβ were the only cytokines that were consistently able to induce *Cxcl13* transcripts in lung fibroblasts (Fig. 6 C), suggesting they may be important factors that promote pulmonary *Cxcl13* expression in vivo.

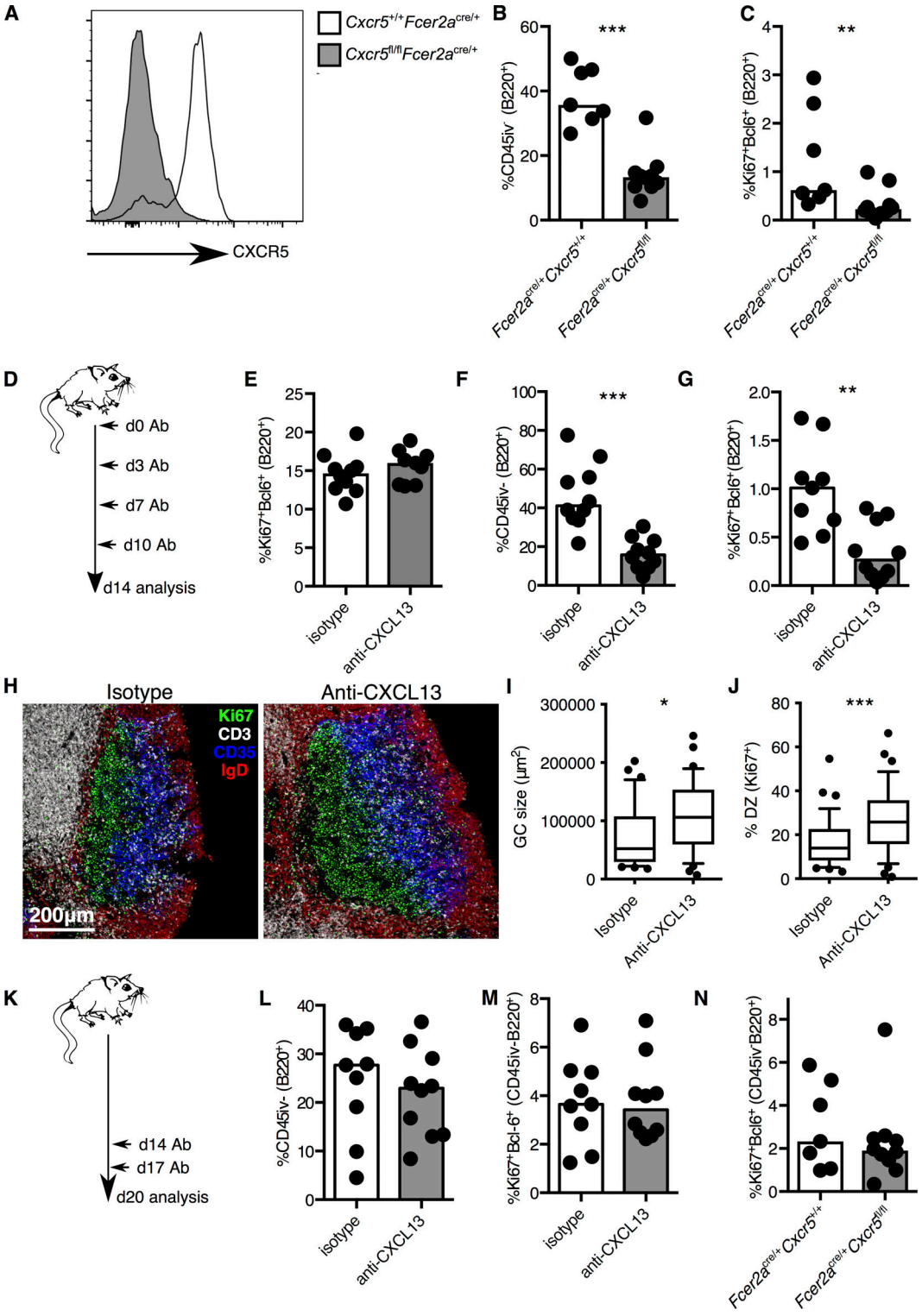

Figure 4. **B cell–intrinsic CXCR5 expression is required to establish a lung GC response but is dispensable for its maintenance. (A)** Flow cytometric histogram of CXCR5 expression on lung CD19$^+$B220$^+$ B cells from *Cxcr5*$^{fl/fl}$ *Tg(Fcer2a*^{cre}*)* mice and *Cxcr5*$^{+/+}$ *Tg(Fcer2a*^{cre}*)* control mice 14 d after IAV infection. **(B and C)** Quantification of CD45i.v.$^-$B220$^+$ (B) and Ki67$^+$Bcl6$^+$B220$^+$ GC B cells (C) in the lung parenchyma 14 d after IAV infection of *Cxcr5*$^{fl/fl}$ *Tg(Fcer2a*^{cre}*)* mice and *Cxcr5*$^{+/+}$ *Tg(Fcer2a*^{cre}*)* control mice. Data are representative of four independent experiments with five to eight mice per group. **(D)** Experimental design of experiment to block CXCL13 through IAV infection. **(E–G)** Proportion of medLN Ki67$^+$Bcl6$^+$B220$^+$ GC B cells (E) and CD45i.v.$^-$B220$^+$ B cells (F) in the lung parenchyma and lung Ki67$^+$Bcl6$^+$B220$^+$ GC B cells (G) in WT mice dosed with anti-CXCL13 antibody or isotype control as shown in D. Data are representative of two independent experiments with 10 mice per group. **(H)** Confocal image of medLNs from mice treated as in D showing the GC as defined by CD3 (white), IgD (red), CD35 (blue), and Ki67 (green) staining. Scale bar, 200 µm. **(I and J)** Analysis of medLN GC structure after anti-CXCL13 administration, quantifying GC size (in square micrometers; I) and the proportion of the GC that is DZ, as defined by Ki67 positivity (J). Data are representative of two independent experiments

with five mice per group. **(K)** Experimental design of the experiment to block CXCL13 after GC formation. **(L and M)** Proportion of CD45i.v.$^-$B220$^+$ B cells in the lung parenchyma (L) and lung Ki67$^+$Bcl6$^+$B220$^+$ GC B cells (M) in C57BL/6 mice dosed with anti-CXCL13 antibody or isotype control as shown in H. Data are representative of two independent experiments with 10 mice per group. **(N)** Frequency of Ki67$^+$Bcl6$^+$B220$^+$ GC B cells within the CD45i.v.$^-$ lung resident B cell population in *Cxcr5*$^{fl/fl}$ *Tg(Fcer2a*^{cre}*)* mice and *Cxcr5*$^{+/+}$ *Tg(Fcer2a*^{cre}*)* control mice 14 d after IAV infection. Data are representative of four independent experiments with five to eight mice per group. In bar plots, the height of the bar is the median, and each symbol represents one biological replicate. In I and J, box and whiskers show the 10th–90th percentile range. P values shown were calculated using a Mann–Whitney *U* test (*, P < 0.05; **, P < 0.01; ***, P < 0.001).

Type I IFN induces Cxcl13 expression in vivo

Type I IFNs are produced by virally infected cells to limit viral spread (Sanders et al., 2011). *Ifnb1* mRNA was induced in CD45$^+$ cells and epithelial cells 5 d after IAV infection (Fig. 6 D), in line with the cell types previously shown to be directly infected by IAV (Sanders et al., 2011). To determine if the type I IFN produced by these cells supports *Cxcl13* induction in the lung during IAV infection, we analyzed whole-lung microarray data from IAV-infected animals that lack the IFNα/β receptor 1 (IFNAR1) and therefore type I IFN signaling (Cilloniz et al., 2010). We examined genes that changed differently over time in control and *Ifnar1*$^{-/-}$ animals and confirmed that the induction of type I IFN responsive genes was impaired in *Ifnar1*$^{-/-}$ mice (Fig. 6 E, top). We then assessed how global chemokine expression was altered using the same unbiased approach. Six chemokines were significantly reduced in the lungs of mice that lacked IFNAR1, with *Cxcl13* being the most affected (Fig. 6 E, bottom). *Cxcl13* mRNA was significantly reduced (by 50%) in the lungs of *Ifnar1*$^{-/-}$ mice 3 d after IAV infection (Fig. 6 F). Although *Ifnar1*$^{-/-}$ mice have reduced expression of *Cxcl13* 3 d after IAV infection, these mice were able to recruit B cells to the lung and form pulmonary GCs 14 d after infection (Fig. S4, A and B). This was also observed in mice lacking IFNAR1 in nonhematopoietic cells (Fig. S4, C and D). *Ifnar1*$^{-/-}$ mice had enhanced production of inflammatory mediators such as *Il1a* (Fig. S4 E), likely caused by excessive viral replication in these mice (Fig. S4 F; Seo et al., 2011). IL-1 has been shown to support iBALT formation in vivo (Kuroda et al., 2016; Neyt et al., 2016), suggesting that redundant mechanisms are in place to ensure iBALT formation during IAV infection.

Combinatorial treatment with IFNβ and cGAMP induces B cell trafficking and pulmonary GC formation in the absence of viral infection

To determine if type I IFN is sufficient to induce *Cxcl13* expression in the lung in vivo, in the absence of viral infection, we administered a single dose of IFNβ i.n. The canonical IFN-inducible gene *Mx1* was induced 24 h after treatment (Fig. 6 G). This single dose of type I IFN was also able to induce *Cxcl13* mRNA in the lung at the same time point (Fig. 6 H), demonstrating that this cytokine can induce pulmonary *Cxcl13* expression. We next sought to determine whether it could also induce B cell trafficking. We administered three doses of IFNβ i.n. at intervals of 2 d (Fig. 7 A) and measured B cell responses on day 6. We found that IFNβ alone did not induce significant B cell trafficking into the lung (Fig. 7 B), despite CXCL13 being the key chemokine for B cell recruitment during IAV infection (Fig. 4). We hypothesized that this may be because B cells require a second signal, in addition to chemokines, to be retained in the lung after recruitment. As B cells can be recruited to the lung parenchyma without BCR triggering (Fig. 3 D) a second signal was likely to be delivered by a pathogen- or danger-associated signal. To test this, we coadministered IFNβ with 2′3′-cyclic GMP-AMP (cGAMP), a nucleoside analogue that can potentiate B cell activation via the STING pathway (Walker et al., 2018), using the same experimental protocol as in Fig. 7 A. While IFNβ or cGAMP alone could not induce B cell trafficking, the combination of these molecules induced significant influx of B cells into the lung parenchyma (Fig. 7 C). We then determined whether this combination therapy was sufficient to induce pulmonary GCs. To this end, we administered the model immunogen NP-KLH with or without IFNβ and/or cGAMP for 3 d and determined the development of medLN and pulmonary GCs 14 d after the first dose. The combination of IFNβ and cGAMP induced strong GC responses in both the medLN and the lung, including the development of antigen-specific NP$^+$IgG1$^+$ GC B cells (Fig. 7 D). We found striking differences in the capacity of these stimulants to induce pulmonary and medLN GCs: while IFNβ, cGAMP, and the combination could induce some medLN GC formation, only the combination of IFNβ and cGAMP was able to induce pulmonary GC formation, in line with the requirement for both of these molecules to induce B cell trafficking to this tissue. These data demonstrate that the requirements for SLO and ectopic GC formation are distinct, perhaps explaining the differences in GC output from these two sites (Adachi et al., 2015).

Discussion

In the humoral response to IAV, the induction of broadly neutralizing cross-reactive antibodies has excellent therapeutic potential, as this may provide protection against multiple IAV strains. How the immune system balances the generation of highly specific and cross-reactive antibodies is, however, poorly understood. The formation of pulmonary GCs following IAV infection is sufficient to protect against subsequent infection (Moyron-Quiroz et al., 2004), demonstrating the potency of this local immune response. Mice that lack SLOs also survive higher doses of IAV infection, suggesting that the inflammation induced in the lung alone is less pathogenic than the systemic immune response (Moyron-Quiroz et al., 2004, 2006). Differences in output from SLO GCs compared with pulmonary GCs during IAV infection (Adachi et al., 2015) suggest that anatomical location may impact on GC quality. Here, we have shown that type I IFN, produced by infected epithelial cells to combat viral spread (Sanders et al., 2011), also coordinates the local adaptive immune response in the lung. CXCL13 expression is induced in lung fibroblasts by type I IFN signaling and this in turn facilitates the

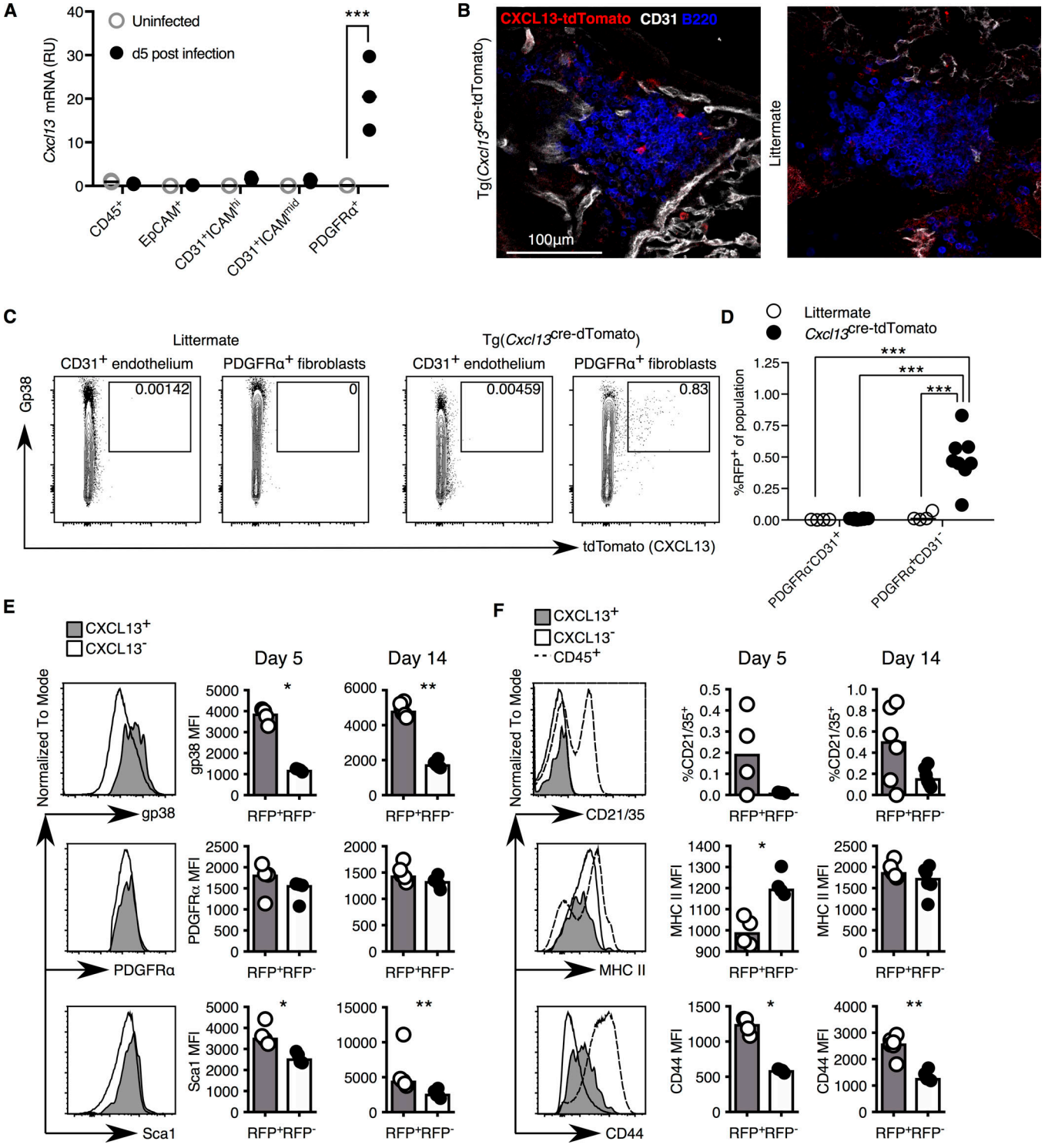

Figure 5. **IAV infection induces CXCL13 in pulmonary PDGFRα⁺ fibroblasts. (A)** Quantitative RT-PCR analysis of *Cxcl13* in the indicated cell populations purified from the uninfected lung or lung 5 d after IAV infection. Data are representative of two independent experiments with three mice per group. **(B–D)** Confocal images (B) of CXCL13-tdTomato (red), CD31 (white), and B220 (blue) and flow cytometry quantification (C and D) of CXCL13-expressing cells in lung tissue 5 d after IAV infection of Tg(*Cxcl13*$^{cre\text{-}dTomato}$) or littermate control mice. Scale bar, 100 µm. Numbers in C indicate the proportion of RFP⁺ cells within the indicated populations. Data are representative of three independent experiments with four to eight mice per group. **(E and F)** Flow cytometric phenotyping of CD45⁻CD31⁻PDGFRα⁺CXCL13⁺ (gray) and CXCL13⁻ (white) cells isolated 5 and 14 d after IAV infection from lung alongside CD45⁺ cells for staining reference (F only, dashed line). The expression of gp38, PDGFRα, or Sca1 (E) and CD21/35, MHC II, or CD44 (F) in the indicated populations was determined by mean fluorescence intensity (MFI) of staining or proportion of cells expressing the marker (CD21/35 only). Data are representative of three independent experiments with four to six mice per group. P values in A and D were calculated using a two-way ANOVA. P values in E and F were calculated using a Mann–Whitney *U* test. *, P < 0.05; **, P < 0.01; ***, P < 0.001.

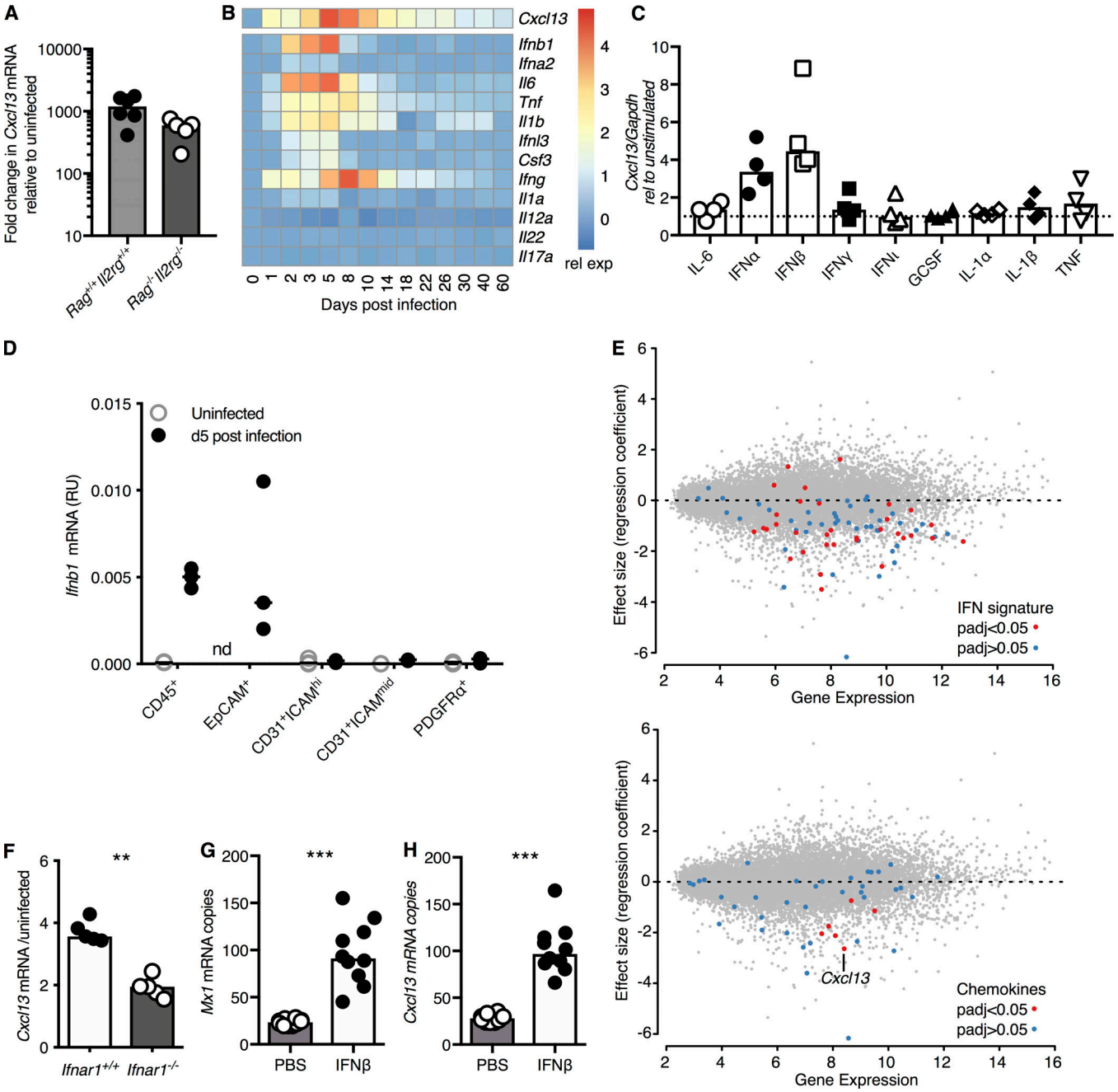

Figure 6. **Type I IFN induces *Cxcl13* expression in the lung in vivo. (A)** *Cxcl13* induction in whole-lung mRNA in *Rag2*$^{-/-}$*Il2rg*$^{-/-}$ and *Rag2*$^{+/+}$*Il2rg*$^{+/+}$ WT control mice 5 d after IAV infection. Data are representative of two independent experiments with five or six mice per group. **(B)** Heat map of cytokine mRNA expression from a whole-lung microarray dataset at the indicated days after IAV infection. Expression for each probeset is shown relative to mock-infected animals. Data were reanalyzed from a previously published dataset (Pommerenke et al., 2012). **(C)** Quantitative RT-PCR analysis of *Cxcl13* in lung fibroblasts stimulated with the indicated cytokine for 6 h in vitro, the dotted line indicates a fold change of one over unstimulated cells. In all dot plots, each symbol represents an independent biological replicate, and data are representative of three independent experiments with four mice per group. **(D)** Quantitative RT-PCR analysis of *Ifnb1* in the indicated cell populations purified from the uninfected lung, or lung 5 d after IAV infection. *Ifnb1* level is represented as expression relative to *Gapdh* in each cell type; nd, not detected. Data are representative of two independent experiments with three mice per group. **(E)** Regression coefficients for each gene are plotted against mean normalized gene expression values (change from day 1 to day 3; WT vs. *Ifnar1*$^{-/-}$). IFN-responsive (top) or chemokine (bottom) genes are highlighted in blue ($P > 0.05$) or red ($P < 0.05$; F test across days 1, 3, and 4, after multiple correction testing). **(F)** Expression of pulmonary *Cxcl13* relative to uninfected animals 3 d after IAV infection as determined by microarray. Data were reanalyzed from a previously published dataset (Cilloniz et al., 2010). **(G and H)** Quantitative RT-PCR for *Mx1* (G) and *Cxcl13* (H) in whole-lung mRNA samples taken 24 h following i.n. administration of IFNβ. Data are representative of two independent experiments with ten mice per group. For two-way comparisons, P values shown were calculated using a Mann–Whitney *U* test. **, $P < 0.01$; ***, $P < 0.001$. In all dot plots, each symbol represents an independent biological replicate.

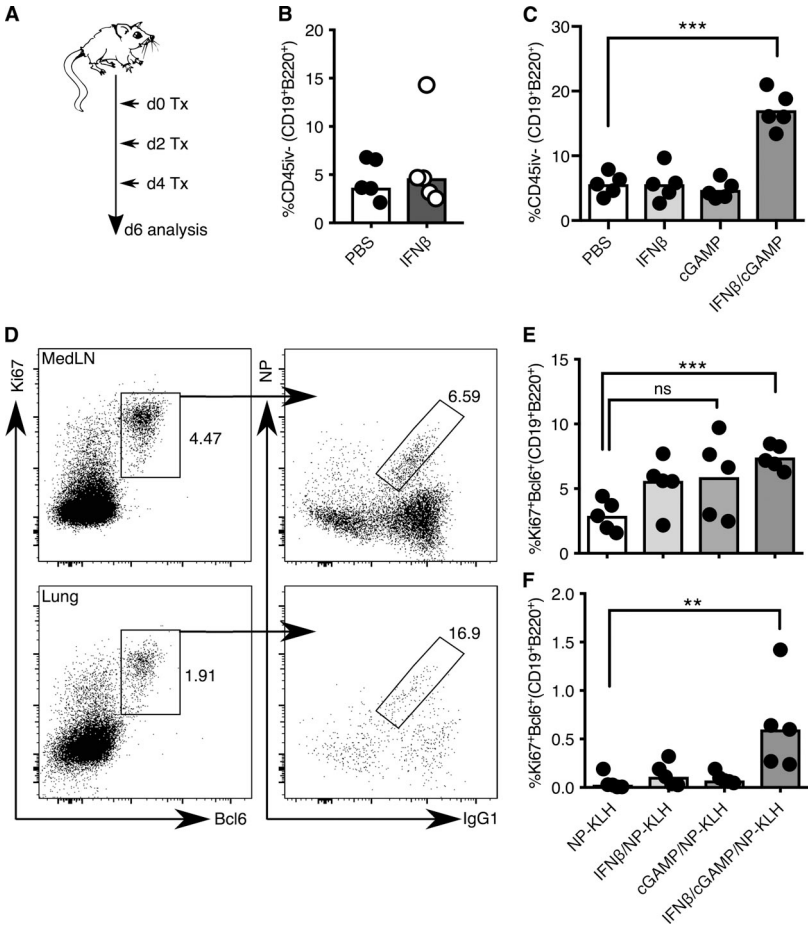

Figure 7. **IFNβ combined with cGAMP induces B cell trafficking and pulmonary GCs. (A and B)** WT mice were administered IFNβ i.n. on days 0, 2, and 4 (A), and the ability of B cells to enter the lung parenchyma was determined on day 6 by i.v. anti-CD45 labeling (B). Data are representative of four independent experiments with five mice per group. **(C)** WT mice were treated with IFNβ and/or cGAMP i.n. as in A, and the proportion of B cells that had entered the lung parenchyma was determined by anti-CD45i.v. labeling. Data are representative of two independent experiments with five mice per group. **(D–F)** WT mice were administered NP-KLH with IFNβ and/or cGAMP i.n. on days 0, 1, and 2, and the development of GCs was determined in the lung and medLN 14 d after the first dose. GC B cell staining (D) in medLN (top) and lung (bottom) is shown for mice administered NP-KLH/IFNβ/cGAMP, determined by Bcl6 and Ki67 expression on $B220^+CD19^+CD45^+$ cells. Antigen specificity was also demonstrated by costaining for NP and IgG1 on GC B cells ($CD45^+CD19^+B220^+Bcl6^+Ki67^+$). Numbers in flow plots (D) indicate the proportion of GC B cells among B cells and the proportion of GC B cells that are antigen specific. The proportion of GC B cells was also determined in the medLN (E) and lung (F) in all treatment groups. Data are representative of two independent experiments with five mice per group. P values were calculated using a two-way ANOVA test, and each symbol represents a biological replicate. **, $P < 0.01$; ***, $P < 0.001$; ns, not significant.

CXCR5-dependent recruitment of B cells to the lung to initiate a GC response. Moreover, administration of type I IFN in conjunction with a second signal drives recruitment of B cells into the lung parenchyma and is sufficient for the formation of functional pulmonary GCs. The formation of functional GCs in the lung, in parallel with those in SLOs, at first glance appears to be an energetically expensive duplication of effort. However, analysis of the lung B cell repertoire after IAV infection reveals different antibody repertoire usage at this site compared with the LN, one that would generate more broadly neutralizing antibodies (Adachi et al., 2015; Takahashi et al., 2017). Together, this suggests that compounds that stimulate a type I IFN response may be useful as vaccine adjuvants to generate cross-protective B cell responses at mucosal sites.

While it is clear that GC responses in TLSs are qualitatively different from those in SLOs, how this difference in B cell receptor repertoire is generated is not clear. Here, we show that c-Myc is induced in fewer lung GC B cells than medLN GC B cells, indicating alterations in positive selection in the lung. This might be due to impaired access to antigen, reduced specific antigen display among a broader range of antigens, or reduced T cell help. This may also be the cause of the increased proportion of LZ phenotype GC B cells in the lung, as fewer cells may receive cues that would prompt them to acquire a DZ phenotype. Impaired selection of GC B cells in the lung may occur because the structure of ectopic GC is not as organized as that of the GC in SLOs (Moyron-Quiroz et al., 2004, 2006; Denton and Linterman, 2017), making access to Tfh cells and/or immune complexes less likely. Limitations of either or both signals would alter the selection of B cells that emerge from the GC as long-lived plasma cells or memory B cells, thereby altering the repertoire of effector B cells produced in the lung.

Our results indicate that the IAV infection–induced remodeling of lung fibroblasts makes them functionally resemble the CXCL13-producing FDCs in the B cell follicle of SLOs. It is clear from our data that pulmonary $CXCL13^+$ fibroblasts are not FDCs, despite the detection of rare $CD35^+$ FDC-like cells in pulmonary GCs, and are phenotypically distinct from pulmonary $CXCL13^-$ fibroblasts; lung $CXCL13^+$ fibroblasts do not express the canonical FDC marker CD21/35 and have differential cell-surface expression of gp38, MHC II, Sca1, and CD44. CXCL13-expressing cells that do not express CD35 have been observed in pulmonary adenocarcinoma–associated TLSs (Joshi et al., 2015) and in the omentum (Rangel-Moreno et al., 2009). These data suggest that the pathway that induces CXCL13 expression in inflammatory conditions is distinct from that which supports LN FDCs. Indeed, signaling through the lymphotoxin-β receptor (LTβR) is critical to the formation and maintenance of the LN FDC network that supports the B cell follicle and GC formation, as these structures are unstable in mice with disrupted LTβR signaling (Brendolan and Caamaño, 2012) and poorly organized in mice that lack the LTβR on LN mesenchymal stromal cells (Onder et al., 2017). By

contrast, induction of CXCL13 in the lung after IAV infection occurs independently of lymphotoxin signaling (Moyron-Quiroz et al., 2004) and LTi cells (Rangel-Moreno et al., 2011), demonstrating that there are distinct pathways responsible for initiating de novo CXCL13 expression in adulthood. The induction of CXCL13 by type I IFN, reported here, is one such mechanism.

Type I IFN is not the only cytokine able to induce CXCL13 in nonlymphoid tissues. In response to particulate antigens and viral infection, CXCL13 can be induced in lung fibroblasts via IL-1 signaling (Kuroda et al., 2016; Neyt et al., 2016), by IL-22 in the salivary gland in a mouse model of Sjögren's syndrome (Barone et al., 2015), or in the fat by TNF (Bénézech et al., 2015). Furthermore, treatment of neonates with LPS results in CXCL13 induction and iBALT formation in an IL-17-dependent fashion (Rangel-Moreno et al., 2011). Together, these studies highlight the fact that multiple pathways have the potential to induce pulmonary CXCL13 expression. Such redundancy in biological systems is common and may have evolved to ensure that TLSs are able to form in response to a number of infections that may induce a different inflammatory environment.

While this study focused on the generation of pulmonary GCs during IAV infection, ectopic GCs have been described in a number of inflammatory disorders, including multiple antibody-mediated autoimmune disorders (Psarras et al., 2017), cancer, and COPD. In COPD patients, there is a positive correlation between CXCL13 expression and B cell accumulation in the lung (Hogg et al., 2004), suggesting that a CXCL13-dependent mechanism of B cell recruitment occurs in human disease. While the link between type I IFN and TLS formation is difficult to test in humans, there are a number of autoimmune diseases that have been described as having an "IFN signature," in which excessive type I IFN activity is a key feature of disease. These include systemic lupus erythematosus, insulin-dependent diabetes mellitus, rheumatoid arthritis, Sjögren's syndrome, dermatomyositis, systemic sclerosis (Rönnblom and Eloranta, 2013), and the rare, lupus-like monogenic interferonopathies (Rodero and Crow, 2016). Whether the IFN in these conditions is pathogenic or a consequence of disease remains unresolved, although IFN blockade trials are ongoing (Psarras et al., 2017). The majority of diseases with an IFN signature do, however, have autoantibodies and GC-containing ectopic lymphoid tissue within the target tissues (Pitzalis et al., 2014). This, together with the work presented here, suggests that type I IFN may trigger the formation of GC-containing TLSs in autoimmune disease. Perturbation of this axis, either by IFN or CXCL13 blockade, has promise in the treatment of a panoply of autoimmune and inflammatory diseases, while stimulation of this system via intranasal vaccination may promote protective immunity.

Materials and methods

Mice, infections, treatments, and in vivo labeling

Mice on the C57BL/6 background used in this study were derivatives of the following: *Tcra*$^{-/-}$, *Cd4*^{cre}, *Cxcr5*$^{fl/fl}$ (Bradford et al., 2017), *Bcl6*$^{fl/fl}$, *Aicda*$^{cre\text{-}hCD2}$, *Tbx21*$^{fl/fl}$, Tg(*Fcer2a*^{cre}), *Cmyc*^{GFP}, *Rag2*$^{-/-}$, Tg(*Cxcl13*$^{cre\text{-}dTomato}$), *Prdm1*$^{GFP/+}$, and SW_{HEL} mice. *Cxcr3*$^{fl/fl}$ conditionally deleted mice were generated as described previously (Piovesan et al., 2017). All mice were between 8 and 14 wk of age at the start of the experiment, and both male and female mice were used. No significant differences were observed between the sexes. For experiments using cre-driven transgenic animals, control mice were age- and sex-matched cousins unless otherwise indicated. Mice were bred and maintained in specific-pathogen–free conditions in the Biological Services Unit, Babraham Research Campus. All procedures performed in the UK were approved by the Animal Welfare and Ethical Review Body of the Babraham Research Campus and the UK Home Office. Experiments using *Cxcr3*$^{fl/fl}$ *Tg(Fcer2a*^{cre}*)* mice and controls were performed at the Walter and Eliza Hall Institute. These animal procedures were approved by both WEHI and Monash University Animal Ethics Committees. Mice were administered 10^4 plaque-forming units of influenza A/Hong Kong/1/1968/x31 (x31) virus, 4 × 10^5 IU Betaferon (IFNβ; Bayer), 100 µg NP-KLH (BioSearch Technologies), and/or or 2 µg cGAMP (SML1229; Sigma) i.n. under inhalation anesthesia. Circulating hematopoietic cells were labeled in vivo by i.v. administration of 3 µg biotinylated- or APC-conjugated CD45 (30-F11; BioLegend) antibody 3 min before euthanasia, followed by ex vivo detection with fluorochrome-conjugated streptavidin where appropriate. For antibody blocking experiments, mice were administered 56 mg/kg anti-CXCL13 or isotype control antibody (Vaccinex) i.p. as indicated in the text. For inhibition of LN egress, mice were administered 200 µg FTY720 (Cayman) i.p. 3 and 5 d after IAV infection. For preparation of BM chimeras, *Rag2*$^{-/-}$ recipient mice were sublethally irradiated with 750 rad and reconstituted via i.v. injection with 2 × 10^6 donor BM cells. Chimeric mice were infected with IAV 8 wk after irradiation and cell transfer. For BM chimeras in which all B cells lack CCR7 expression (B:*Ccr7*$^{-/-}$), CD45.1$^+$ *Rag2*$^{-/-}$ mice were irradiated and reconstituted with mixed BM comprising 75% CD45.1$^+$ µMT and 25% CD45.2$^+$ CCR7-deficient BM. Control chimeras were CD45.1$^+$ *Rag2*$^{-/-}$ mice irradiated and reconstituted with mixed BM comprising 75% CD45.1$^+$ µMT and 25% CD45.2$^+$ C57BL/6 BM.

Flow cytometry

LN samples were pressed through a 40-µm mesh before antibody staining in PBS/2% FCS. Lung samples were minced with scissors then forced through a 70-µm mesh before antibody staining. For detection of transcription factors and other intracellular proteins, cells were fixed and permeabilized with Foxp3 fix/perm kit (eBioscience). Antibodies were from eBioscience, BioLegend, or BD Biosciences, unless indicated otherwise, and directed against CD4 (Rm4-5, GK1.5), B220 (RA3-6B2), Foxp3 (FJK-16s), T-bet (eBio4B10), CD19 (6D5), CD138 (281–2), CXCR5 (L138D7), Bcl6 (K112-91), CXCR3 (CXCR3-173), Ki67 (Sol1a1), CXCR4 (L276F12), CD8 (145-2C11), CD11b (M1/70), EpCAM (G8.8), PDGFRα (APA5), CD31 (MEC13.3), ICAM (YN1/1.7.4), CD45 (30-F11), CD86 (GL-1), GL7 (GL7), CD95 (Jo2), MHC II (M5/114.15.2), PD-1 (J43), Sca1 (D7), CD44 (IM7), CD90.2 (30-H12), IL-7Rα (A7R34), IgG1 (A85-1), NP (N-5070-1; Biosearch Technologies), and human CD2 (RPA-2.10). Dead cells were excluded with fixable viability dyes (e780; eBioscience; and Zombie UV;

BioLegend) or DAPI (Sigma). HEL-binding B cells were detected as described previously (Brink et al., 2015).

Microscopy

Lungs were inflated with a 1:1 mix of periodate-lysine-paraformaldehyde with optimal cutting temperature compound and fixed in periodate-lysine-paraformaldehyde for 5 h at 4°C and then embedded in optimal cutting temperature medium. Lung sections were cut at 30 µm, air dried overnight, and then stored at −20°C. Prior to staining, lung sections were further dried for 2 h at 37°C, rehydrated, and blocked with 1% BSA (Sigma) and, where appropriate, 5% goat serum (Sigma). For detection of biotinylated antibodies, endogenous biotin was blocked (Vectorlabs). Sections were stained with B220-488 or -BV421 (RA3-6B2; BioLegend), CD3-APC (17A2; eBioscience), CD31-594 or -biotin (MEC13.3; BioLegend), CD35-biotin (8C12; BD Biosciences), Ki67-FITC (eBioscience), and/or biotinylated anti-hCD2 (RPA-2.10; eBioscience). Biotinylated antibodies were detected with streptavidin-BV421 (BioLegend) or -647 (eBioscience). Images were acquired using a Zeiss LSM780 harboring 405-, 488-, 561-, and 633-nm lasers. Channels were collected in separate frames using 20×/0.50 NA air or 40×/1.40 NA oil lenses. Images were analyzed and compiled using Fiji (National Institutes of Health) software. For analysis of medLN GC structure, 10× tiled images of whole LNs were collected, and GC size was determined by manually outlining the GC area (as indicated by lack of IgD staining) and measuring the area (in square micrometers) using Fiji software. For analysis of the DZ area, the Ki67 stain was converted to a binary image after thresholding and the proportion of the manually-defined GC area that was $Ki67^+$ was calculated using Fiji software. Values were calculated for individual GCs in each section and averaged across all mice in each group.

Whole-lung RNA analysis

Whole lungs or single lobes were homogenized in 2 ml or 1 ml Trizol (Life Technologies), respectively. RNA from 1 ml was extracted as per manufacturer's instructions, keeping volumes strictly equal between samples. Analysis of mRNA expression was determined using equal volumes of starting material and TaqMan primer probes (Applied Biosystems) using the RNA-to-Ct kit (Applied Biosystems), Luna Universal Probe qPCR kit (New England BioLabs), or TaqMan Universal PCR kit (Applied Biosystems) following cDNA generation with random hexamers (ThermoFisher). Ct values were arbitrarily converted to copy number per whole lung or lobe using the equation $10^5 = 2^{(Ct-17)}$, wherein a Ct value of 17 is equivalent to 10^5 copies.

Cell sorting and RNA analysis

Lung stromal cells were isolated as previously described (Denton et al., 2014) and stained for EpCAM (G8.8), CD31 (MEC13.3), CD45 (30-F11), PDGFRα (APA5), and ICAM (YN1/1.7.4), sorted on a BD Influx and RNA extracted using the RNEasy Micro kit (Qiagen). Quantitative real time PCR was performed for *Cxcl3* (Mm0044533_m1), *Ccl19* (Mm00839967_g1), *Ifnb1* (Mm00439552_s1) and *Mx1* (Mm00487796_m1) using the indicated TaqMan primer probes and the RNA-to-Ct kit (Applied Biosystems) and expression normalized to *Gapdh* (Mm99999915_g1) or *Hprt* (Mm03024075_m1).

Lung fibroblast cell culture

Lung stromal cells were isolated by digestion and cultured on tissue culture–treated plates at 37°C 5% CO_2 in RPMI supplemented with 10% FCS, penicillin, and streptomycin. Non-adherent cells were removed by manual disruption 24 and 72 h after plating, thus maintaining adherent fibroblasts in culture. Prior to stimulation, fibroblasts were washed with RPMI/10% FCS and then stimulated with IL-1α (200 ng/ml; Peprotech), IL-1β (200 ng/ml; Peprotech), IL-6 (200 ng/ml; Peprotech), IFNα (1,000 U/ml; pbl assay sciences), IFNβ (1.6×10^4 U/ml; Bayer), G-CSF (200 ng/ml; Peprotech), or TNF (200 ng/ml; Peprotech) for 6 h in media lacking antibiotics. RNA was extracted using the Trizol method and transcripts quantified as described previously (Denton et al., 2014), with *Cxcl13* expression determined relative to *Gapdh* or *Hprt* and then normalized to unstimulated cells.

Microarray analysis

For the analysis of whole-lung transcriptome over the course of IAV infection, publicly available Robust Multiarray Averaging (RMA)–normalized data were downloaded from the ArrayExpress database (accession no. E-MTAB-764). This dataset is a time course of the transcriptomes of whole lungs in C57BL/6 mice infected with IAV (strain A/Puerto Rico/8/1934 H1N1; Pommerenke et al., 2012). The heat map was generated using probes matching our curated gene list. Each probe was summarized using a mean difference from mock-infected samples. In brief, we first corrected RMA expression values from each probe using the mean expression in mock-infected samples. Second, biological replicates of each time point were averaged using means. For *Ifng* and *Il1a*, there were two matching probes, which behaved similarly; for clarity only one was plotted. The analysis was performed in RStudio (version 1.0.153)/R version 3.4.1; https://www.R-project.org/) using the following packages: Bioconductor (Biobase version 2.36.2), ArrayExpress (1.36.1), pheatmap (1.0.9), and gridSVG (1.6–0), with Bioconductor's microarray annotation package mgug4122a.db (3.2.3).

For analysis of global gene expression changes in *Ifnar1*$^{-/-}$ and WT animals, raw data were downloaded from the Gene Expression Omnibus database (accession no. GSE48890). Agilent data were imported in R, using read.maimages from the limma package (3.32.10) and normalized using the variance stabilization normalization. Sample annotation data (in sdrf format) were downloaded from the corresponding ArrayExpress record. This experiment measured whole-lung transcriptomes at days 1, 3, and 4 after i.n. infection with either r1918 or VN1203 influenza virus in both WT and *Ifnar1*$^{-/-}$ animals (Cilloniz et al., 2010). Limma was performed using the dye-swap pairs for each sample, with the following contrasts: difference day 3 = (*Ifnar1*$^{-/-}$ day 3 − *Ifnar1*$^{-/-}$ day 1) − (WT day 3 − WT day 1) and difference day 4 = (*Ifnar1*$^{-/-}$ day 4 − *Ifnar1*$^{-/-}$ day 3) − (WT day 4 − WT day 3). This seeks to find genes that are significantly different between *Ifnar1*$^{-/-}$ and WT over time, i.e., genes where the response is lost or gained by the absence of IFNAR1. P values from F tests on

these linear models were used after Benjamini–Hochberg multiple correction testing. We did not separate r1918 from VN1203 for this analysis. We used the "HALLMARK_INTERFERON_ALPHA_RESPONSE" gene set defined by the molecular signatures database (http://software.broadinstitute.org/gsea/msigdb/cards/HALLMARK_INTERFERON_ALPHA_RESPONSE.html). This is a computationally generated gene set based on concordance between various IFN stimulation gene expression experiments. To define chemokines, we used two gene ontology (GO) terms: GO:0048020 = CCR chemokine receptor binding and GO:0045236 = CXCR chemokine receptor binding. These were mapped to gene symbols using Bioconductor annotation package org.Mm.eg.db (3.4.1). *Cxcl13* expression at day 3 used normalized data from a single dye swap (day 3 postinfection cDNA labeled with Cy5, uninfected cDNA labeled with Cy3).

Statistical analysis

Single comparisons were analyzed using the nonparametric Mann–Whitney *U* test. Multiple comparisons were performed using ANOVA with Bonferroni multiple testing correction. All statistical analyses were performed with GraphPad Prism, unless otherwise indicated.

Online supplemental material

Fig. S1 shows the expression of GL-7 and CD95, the CD45i.v. labeling of pulmonary GC B cells, and the presence of pulmonary plasma cells. Fig. S2 shows the role of Tfh cells and B cell–expressed CXCR3 in B cell migration to the lung 6 d after IAV infection. Fig. S3 is the gating strategy for identifying stromal cell populations in the lung. Fig. S4 shows B cell trafficking, lung GC formation, and enhanced viral load in IFNAR1-deficient mice.

Acknowledgments

We thank M. Turner, G. Butcher, and A. Liston for their critical reading of this manuscript, M. Busslinger (Research Institute of Molecular Pathology) for the *Tg(Fcer2a^{cre})* mice, and staff within the Biological Support Unit, Imaging Facility and Flow Cytometry Facility at the Babraham Institute for research support. In particular, we would like to acknowledge Carly Noble and Nicola Evans-Bailey for excellent animal husbandry throughout the IAV infection studies. We are grateful to Vaccinex for providing the anti-CXCL13 and isotype control antibody for use in this study.

This study was supported by the Biotechnology and Biological Sciences Research Council (grants BBS/E/B/000C0407 and BBS/E/B/000C0427), Core Capability Grant funding to the Babraham Institute Facilities, and the National Health and Medical Research Council (project grant 1137989 to J.R. Groom and K.L. Good-Jacobson and project grant 1057707 to K.L. Good-Jacobson). A.E. Denton is supported by the Biotechnology and Biological Sciences Research Council (Future Leader Fellowship BB/N011740/1). Development of the *Cxcr5$^{fl/fl}$* (strain *Cxcr5$^{tm1.Namt}$*) was supported by the Biotechnology and Biological Sciences Research Council (grants BB/F019726/1 and BBS/E/D/20002174 to N.A. Mabbott and B.M. Bradford). F. Lafouresse is supported by a Walter and Eliza Hall Centenary Fellowship. J.R. Groom is supported by the Australian Research Council (Future Fellowship FT130100708). K.L. Good-Jacobson is supported by the National Health and Medical Research Council (Career Development Fellowship 1108066).

The authors declare no competing financial interests.

Author contributions: A.E. Denton and M.A. Linterman designed the study, performed experiments, analyzed results, and wrote the manuscript. S. Innocentin and F. Lafouresse performed experiments and analyzed results. E.J. Carr did the microarray analyses and contributed to writing the manuscript. J.R. Groom and K.L. Good-Jacobson designed experiments and analyzed data. B.M. Bradford, U. Mörbe, N.A. Mabbott, and B. Ludewig provided novel mouse strains for this project. All authors read, edited, and approved the manuscript.

Submitted: 28 June 2018
Revised: 5 December 2018
Accepted: 17 January 2019

References

Acton, S.E., A.J. Farrugia, J.L. Astarita, D. Mourão-Sá, R.P. Jenkins, E. Nye, S. Hooper, J. van Blijswijk, N.C. Rogers, K.J. Snelgrove, et al. 2014. Dendritic cells control fibroblastic reticular network tension and lymph node expansion. *Nature.* 514:498–502. https://doi.org/10.1038/nature13814

Adachi, Y., T. Onodera, Y. Yamada, R. Daio, M. Tsuiji, T. Inoue, K. Kobayashi, T. Kurosaki, M. Ato, and Y. Takahashi. 2015. Distinct germinal center selection at local sites shapes memory B cell response to viral escape. *J. Exp. Med.* 212:1709–1723. https://doi.org/10.1084/jem.20142284

Anderson, K.G., H. Sung, C.N. Skon, L. Lefrancois, A. Deisinger, V. Vezys, and D. Masopust. 2012. Cutting edge: intravascular staining redefines lung CD8 T cell responses. *J. Immunol.* 189:2702–2706. https://doi.org/10.4049/jimmunol.1201682

Barone, F., S. Nayar, J. Campos, T. Cloake, D.R. Withers, K.M. Toellner, Y. Zhang, L. Fouser, B. Fisher, S. Bowman, et al. 2015. IL-22 regulates lymphoid chemokine production and assembly of tertiary lymphoid organs. *Proc. Natl. Acad. Sci. USA.* 112:11024–11029. https://doi.org/10.1073/pnas.1503315112

Bénézech, C., N.T. Luu, J.A. Walker, A.A. Kruglov, Y. Loo, K. Nakamura, Y. Zhang, S. Nayar, L.H. Jones, A. Flores-Langarica, et al. 2015. Inflammation-induced formation of fat-associated lymphoid clusters. *Nat. Immunol.* 16:819–828. https://doi.org/10.1038/ni.3215

Bradford, B.M., B. Reizis, and N.A. Mabbott. 2017. Oral Prion Disease Pathogenesis Is Impeded in the Specific Absence of CXCR5-Expressing Dendritic Cells. *J. Virol.* 91: e00124-17. https://doi.org/10.1128/JVI.00124-17

Brendolan, A., and J.H. Caamaño. 2012. Mesenchymal cell differentiation during lymph node organogenesis. *Front. Immunol.* 3:381. https://doi.org/10.3389/fimmu.2012.00381

Brink, R., D. Paus, K. Bourne, J.R. Hermes, S. Gardam, T.G. Phan, and T.D. Chan. 2015. The SW(HEL) system for high-resolution analysis of in vivo antigen-specific T-dependent B cell responses. *Methods Mol. Biol.* 1291:103–123. https://doi.org/10.1007/978-1-4939-2498-1_9

Calado, D.P., Y. Sasaki, S.A. Godinho, A. Pellerin, K. Köchert, B.P. Sleckman, I.M. de Alborán, M. Janz, S. Rodig, and K. Rajewsky. 2012. The cell-cycle regulator c-Myc is essential for the formation and maintenance of germinal centers. *Nat. Immunol.* 13:1092–1100. https://doi.org/10.1038/ni.2418

Cilloniz, C., M.J. Pantin-Jackwood, C. Ni, A.G. Goodman, X. Peng, S.C. Proll, V.S. Carter, E.R. Rosenzweig, K.J. Szretter, J.M. Katz, et al. 2010. Lethal dissemination of H5N1 influenza virus is associated with dysregulation of inflammation and lipoxin signaling in a mouse model of infection. *J. Virol.* 84:7613–7624. https://doi.org/10.1128/JVI.00553-10

Cremasco, V., M.C. Woodruff, L. Onder, J. Cupovic, J.M. Nieves-Bonilla, F.A. Schildberg, J. Chang, F. Cremasco, C.J. Harvey, K. Wucherpfennig, et al. 2014. B cell homeostasis and follicle confines are governed by

fibroblastic reticular cells. *Nat. Immunol.* 15:973–981. https://doi.org/10.1038/ni.2965

Denton, A.E., and M.A. Linterman. 2017. Stromal networking: cellular connections in the germinal centre. *Curr. Opin. Immunol.* 45:103–111. https://doi.org/10.1016/j.coi.2017.03.001

Denton, A.E., E.W. Roberts, M.A. Linterman, and D.T. Fearon. 2014. Fibroblastic reticular cells of the lymph node are required for retention of resting but not activated CD8+ T cells. *Proc. Natl. Acad. Sci. USA.* 111:12139–12144. https://doi.org/10.1073/pnas.1412910111

Dominguez-Sola, D., G.D. Victora, C.Y. Ying, R.T. Phan, M. Saito, M.C. Nussenzweig, and R. Dalla-Favera. 2012. The proto-oncogene MYC is required for selection in the germinal center and cyclic reentry. *Nat. Immunol.* 13:1083–1091. https://doi.org/10.1038/ni.2428

Fleige, H., S. Ravens, G.L. Moschovakis, J. Bölter, S. Willenzon, G. Sutter, S. Häussler, U. Kalinke, I. Prinz, and R. Förster. 2014. IL-17-induced CXCL12 recruits B cells and induces follicle formation in BALT in the absence of differentiated FDCs. *J. Exp. Med.* 211:643–651. https://doi.org/10.1084/jem.20131737

Foo, S.Y., and S. Phipps. 2010. Regulation of inducible BALT formation and contribution to immunity and pathology. *Mucosal Immunol.* 3:537–544. https://doi.org/10.1038/mi.2010.52

Förster, R., A.E. Mattis, E. Kremmer, E. Wolf, G. Brem, and M. Lipp. 1996. A putative chemokine receptor, BLR1, directs B cell migration to defined lymphoid organs and specific anatomic compartments of the spleen. *Cell.* 87:1037–1047. https://doi.org/10.1016/S0092-8674(00)81798-5

Förster, R., A. Schubel, D. Breitfeld, E. Kremmer, I. Renner-Müller, E. Wolf, and M. Lipp. 1999. CCR7 coordinates the primary immune response by establishing functional microenvironments in secondary lymphoid organs. *Cell.* 99:23–33. https://doi.org/10.1016/S0092-8674(00)80059-8

Groom, J.R., and A.D. Luster. 2011. CXCR3 in T cell function. *Exp. Cell Res.* 317:620–631. https://doi.org/10.1016/j.yexcr.2010.12.017

Hogg, J.C., F. Chu, S. Utokaparch, R. Woods, W.M. Elliott, L. Buzatu, R.M. Cherniack, R.M. Rogers, F.C. Sciurba, H.O. Coxson, and P.D. Paré. 2004. The nature of small-airway obstruction in chronic obstructive pulmonary disease. *N. Engl. J. Med.* 350:2645–2653. https://doi.org/10.1056/NEJMoa032158

Huang, C.Y., A.L. Bredemeyer, L.M. Walker, C.H. Bassing, and B.P. Sleckman. 2008. Dynamic regulation of c-Myc proto-oncogene expression during lymphocyte development revealed by a GFP-c-Myc knock-in mouse. *Eur. J. Immunol.* 38:342–349. https://doi.org/10.1002/eji.200737972

Hwang, J.Y., T.D. Randall, and A. Silva-Sanchez. 2016. Inducible Bronchus-Associated Lymphoid Tissue: Taming Inflammation in the Lung. *Front. Immunol.* 7:258. https://doi.org/10.3389/fimmu.2016.00258

Joshi, N.S., E.H. Akama-Garren, Y. Lu, D.Y. Lee, G.P. Chang, A. Li, M. DuPage, T. Tammela, N.R. Kerper, A.F. Farago, et al. 2015. Regulatory T Cells in Tumor-Associated Tertiary Lymphoid Structures Suppress Anti-tumor T Cell Responses. *Immunity.* 43:579–590. https://doi.org/10.1016/j.immuni.2015.08.006

Kelsen, S.G., M.O. Aksoy, M. Georgy, R. Hershman, R. Ji, X. Li, M. Hurford, C. Solomides, W. Chatila, and V. Kim. 2009. Lymphoid follicle cells in chronic obstructive pulmonary disease overexpress the chemokine receptor CXCR3. *Am. J. Respir. Crit. Care Med.* 179:799–805. https://doi.org/10.1164/rccm.200807-1089OC

Klimatcheva, E., T. Pandina, C. Reilly, S. Torno, H. Bussler, M. Scrivens, A. Jonason, C. Mallow, M. Doherty, M. Paris, et al. 2015. CXCL13 antibody for the treatment of autoimmune disorders. *BMC Immunol.* 16:6. https://doi.org/10.1186/s12865-015-0068-1

Kuroda, E., K. Ozasa, B. Temizoz, K. Ohata, C.X. Koo, T. Kanuma, T. Kusakabe, S. Kobari, M. Horie, Y. Morimoto, et al. 2016. Inhaled Fine Particles Induce Alveolar Macrophage Death and Interleukin-1α Release to Promote Inducible Bronchus-Associated Lymphoid Tissue Formation. *Immunity.* 45:1299–1310. https://doi.org/10.1016/j.immuni.2016.11.010

Lim, H.W., and C.H. Kim. 2007. Loss of IL-7 receptor alpha on CD4+ T cells defines terminally differentiated B cell-helping effector T cells in a B cell-rich lymphoid tissue. *J. Immunol.* 179:7448–7456. https://doi.org/10.4049/jimmunol.179.11.7448

Luo, W., F. Weisel, and M.J. Shlomchik. 2018. B Cell Receptor and CD40 Signaling Are Rewired for Synergistic Induction of the c-Myc Transcription Factor in Germinal Center B Cells. *Immunity.* 48:313–326.

Moyron-Quiroz, J.E., J. Rangel-Moreno, K. Kusser, L. Hartson, F. Sprague, S. Goodrich, D.L. Woodland, F.E. Lund, and T.D. Randall. 2004. Role of inducible bronchus associated lymphoid tissue (iBALT) in respiratory immunity. *Nat. Med.* 10:927–934. https://doi.org/10.1038/nm1091

Moyron-Quiroz, J.E., J. Rangel-Moreno, L. Hartson, K. Kusser, M.P. Tighe, K. D. Klonowski, L. Lefrançois, L.S. Cauley, A.G. Harmsen, F.E. Lund, and T.D. Randall. 2006. Persistence and responsiveness of immunologic memory in the absence of secondary lymphoid organs. *Immunity.* 25:643–654. https://doi.org/10.1016/j.immuni.2006.08.022

Nair, H., W.A. Brooks, M. Katz, A. Roca, J.A. Berkley, S.A. Madhi, J.M. Simmerman, A. Gordon, M. Sato, S. Howie, et al. 2011. Global burden of respiratory infections due to seasonal influenza in young children: a systematic review and meta-analysis. *Lancet.* 378:1917–1930. https://doi.org/10.1016/S0140-6736(11)61051-9

Neyt, K., C.H. GeurtsvanKessel, K. Deswarte, H. Hammad, and B.N. Lambrecht. 2016. Early IL-1 Signaling Promotes iBALT Induction after Influenza Virus Infection. *Front. Immunol.* 7:312. https://doi.org/10.3389/fimmu.2016.00312

Okada, T., V.N. Ngo, E.H. Ekland, R. Förster, M. Lipp, D.R. Littman, and J.G. Cyster. 2002. Chemokine requirements for B cell entry to lymph nodes and Peyer's patches. *J. Exp. Med.* 196:65–75. https://doi.org/10.1084/jem.20020201

Onder, L., U. Morbe, N. Pikor, M. Novkovic, H.W. Cheng, T. Hehlgans, K. Pfeffer, B. Becher, A. Waisman, T. Rulicke, et al. 2017. Lymphatic Endothelial Cells Control Initiation of Lymph Node Organogenesis. *Immunity.* 47:80–92.

Onodera, T., Y. Takahashi, Y. Yokoi, M. Ato, Y. Kodama, S. Hachimura, T. Kurosaki, and K. Kobayashi. 2012. Memory B cells in the lung participate in protective humoral immune responses to pulmonary influenza virus reinfection. *Proc. Natl. Acad. Sci. USA.* 109:2485–2490. https://doi.org/10.1073/pnas.1115369109

Oslund, K.L., and N. Baumgarth. 2011. Influenza-induced innate immunity: regulators of viral replication, respiratory tract pathology & adaptive immunity. *Future Virol.* 6:951–962. https://doi.org/10.2217/fvl.11.63

Phan, T.G., M. Amesbury, S. Gardam, J. Crosbie, J. Hasbold, P.D. Hodgkin, A. Basten, and R. Brink. 2003. B cell receptor-independent stimuli trigger immunoglobulin (Ig) class switch recombination and production of IgG autoantibodies by anergic self-reactive B cells. *J. Exp. Med.* 197:845–860. https://doi.org/10.1084/jem.20022144

Piovesan, D., J. Tempany, A. Di Pietro, I. Baas, C. Yiannis, K. O'Donnell, Y. Chen, V. Peperzak, G.T. Belz, C.R. Mackay, et al. 2017. c-Myb Regulates the T-Bet-Dependent Differentiation Program in B Cells to Coordinate Antibody Responses. *Cell Reports.* 19:461–470. https://doi.org/10.1016/j.celrep.2017.03.060

Pitzalis, C., G.W. Jones, M. Bombardieri, and S.A. Jones. 2014. Ectopic lymphoid-like structures in infection, cancer and autoimmunity. *Nat. Rev. Immunol.* 14:447–462. https://doi.org/10.1038/nri3700

Pommerenke, C., E. Wilk, B. Srivastava, A. Schulze, N. Novoselova, R. Geffers, and K. Schughart. 2012. Global transcriptome analysis in influenza-infected mouse lungs reveals the kinetics of innate and adaptive host immune responses. *PLoS One.* 7:e41169. https://doi.org/10.1371/journal.pone.0041169

Psarras, A., P. Emery, and E.M. Vital. 2017. Type I interferon-mediated autoimmune diseases: pathogenesis, diagnosis and targeted therapy. *Rheumatology (Oxford).* 56:1662–1675.

Qi, H., J.L. Cannons, F. Klauschen, P.L. Schwartzberg, and R.N. Germain. 2008. SAP-controlled T-B cell interactions underlie germinal centre formation. *Nature.* 455:764–769. https://doi.org/10.1038/nature07345

Rangel-Moreno, J., L. Hartson, C. Navarro, M. Gaxiola, M. Selman, and T.D. Randall. 2006. Inducible bronchus-associated lymphoid tissue (iBALT) in patients with pulmonary complications of rheumatoid arthritis. *J. Clin. Invest.* 116:3183–3194. https://doi.org/10.1172/JCI28756

Rangel-Moreno, J., J.E. Moyron-Quiroz, L. Hartson, K. Kusser, and T.D. Randall. 2007. Pulmonary expression of CXC chemokine ligand 13, CC chemokine ligand 19, and CC chemokine ligand 21 is essential for local immunity to influenza. *Proc. Natl. Acad. Sci. USA.* 104:10577–10582. https://doi.org/10.1073/pnas.0700591104

Rangel-Moreno, J., J.E. Moyron-Quiroz, D.M. Carragher, K. Kusser, L. Hartson, A. Moquin, and T.D. Randall. 2009. Omental milky spots develop in the absence of lymphoid tissue-inducer cells and support B and T cell responses to peritoneal antigens. *Immunity.* 30:731–743. https://doi.org/10.1016/j.immuni.2009.03.014

Rangel-Moreno, J., D.M. Carragher, M. de la Luz Garcia-Hernandez, J.Y. Hwang, K. Kusser, L. Hartson, J.K. Kolls, S.A. Khader, and T.D. Randall. 2011. The development of inducible bronchus-associated lymphoid tissue depends on IL-17. *Nat. Immunol.* 12:639–646. https://doi.org/10.1038/ni.2053

Rodero, M.P., and Y.J. Crow. 2016. Type I interferon-mediated monogenic autoinflammation: The type I interferonopathies, a conceptual overview. *J. Exp. Med.* 213:2527–2538. https://doi.org/10.1084/jem.20161596

Rönnblom, L., and M.L. Eloranta. 2013. The interferon signature in autoimmune diseases. *Curr. Opin. Rheumatol.* 25:248–253. https://doi.org/10.1097/BOR.0b013e32835c7e32

Sanders, C.J., P.C. Doherty, and P.G. Thomas. 2011. Respiratory epithelial cells in innate immunity to influenza virus infection. *Cell Tissue Res.* 343: 13–21. https://doi.org/10.1007/s00441-010-1043-z

Seo, S.U., H.J. Kwon, H.J. Ko, Y.H. Byun, B.L. Seong, S. Uematsu, S. Akira, and M.N. Kweon. 2011. Type I interferon signaling regulates Ly6C(hi) monocytes and neutrophils during acute viral pneumonia in mice. *PLoS Pathog.* 7:e1001304. https://doi.org/10.1371/journal.ppat.1001304

Somes, M.P., R.M. Turner, L.J. Dwyer, and A.T. Newall. 2018. Estimating the annual attack rate of seasonal influenza among unvaccinated individuals: A systematic review and meta-analysis. *Vaccine.* 36: 3199–3207. https://doi.org/10.1016/j.vaccine.2018.04.063

Takahashi, Y., T. Onodera, Y. Adachi, and M. Ato. 2017. Adaptive B Cell Responses to Influenza Virus Infection in the Lung. *Viral Immunol.* 30: 431–437. https://doi.org/10.1089/vim.2017.0025

Vinuesa, C.G., M.A. Linterman, D. Yu, and I.C. MacLennan. 2016. Follicular Helper T Cells. *Annu. Rev. Immunol.* 34:335–368. https://doi.org/10.1146/annurev-immunol-041015-055605

Walker, M.M., B.W. Crute, J.C. Cambier, and A. Getahun. 2018. B Cell-Intrinsic STING Signaling Triggers Cell Activation, Synergizes with B Cell Receptor Signals, and Promotes Antibody Responses. *J. Immunol.* 201:2641–2653. https://doi.org/10.4049/jimmunol.1701405

Wang, X., B. Cho, K. Suzuki, Y. Xu, J.A. Green, J. An, and J.G. Cyster. 2011. Follicular dendritic cells help establish follicle identity and promote B cell retention in germinal centers. *J. Exp. Med.* 208:2497–2510. https://doi.org/10.1084/jem.20111449